Assessment of inlet mixing during charge and discharge of a large-scale water pit heat storage

Xiang, Yutong; Gao, Meng; Furbo, Simon; Fan, Jianhua; Wang, Gang; Tian, Zhiyong; Wang, Dengjia

Published in:
Renewable Energy

Link to article, DOI:
10.1016/j.renene.2023.119170

Publication date:
2023

Document Version
Publisher's PDF, also known as Version of record

Renewable Energy 217 (2023) 119170

Contents lists available at ScienceDirect

Renewable Energy

journal homepage: www.elsevier.com/locate/renene

Assessment of inlet mixing during charge and discharge of a large-scale water pit heat storage

Yutong Xiang [a], Meng Gao [a], Simon Furbo [a], Jianhua Fan [a,*], Gang Wang [b], Zhiyong Tian [c], Dengjia Wang [d]

[a] Department of Civil and Mechanical Engineering, Technical University of Denmark, Koppels Allé Building 404, Kgs. Lyngby, DK 2800, Denmark
[b] School of Energy Engineering, Xinjiang Institute of Engineering, Urumqi, 830023, China
[c] School of Environmental Science and Engineering, Huazhong University of Science and Technology, Wuhan, 430074, China
[d] State Key Laboratory of Green Building in Western China, Xi'an University of Architecture and Technology, Xi'an, Shaanxi, 710055, China

ARTICLE INFO

Keywords:
Solar district heating
Water pit heat storage
Three-dimensional model
Inflow mixing
Penetration height
Energy distribution ratio

ABSTRACT

Pit thermal energy storage (PTES) is an efficient renewable energy storage technology widely used in large-scale solar district heating systems. Accurate modeling of mixing in a PTES due to inlet flow is key in calculating heat storage performance. However, the commonly used one-dimensional PTES models fail to consider inlet mixing due to the three-dimensional nature of the mixing flow. This research adopts a three-dimensional model to analyze the dynamic behavior of inlet mixing inside the PTES. The model is validated against measurements of the Dronninglund PTES. To quantify the inlet mixing impact, two performance indicators (i.e., the penetration height (Z) and the energy distribution ratio (η_j)) are proposed. The parametric analysis revealed that Z is more dependent on the Reynold (Re) number than the Froude (Fr) number, while both the Re and Fr numbers influence η_j. According to the dimensional theory, the penetration height Z shows a power-law relation with time. For the energy distribution ratio η_j, a power-law relation with time is seen, although an asymptotic formula is needed in the region of a negative buoyancy jet. Finally, the inflow mixing inside the PTES is characterized under various operating conditions by empirical correlations. The results of this study could be used to improve the current one-dimensional heat storage models in terms of inlet mixing.

1. Introduction

To reduce dependence on traditional fossil energy while achieving net-zero emissions, large-solar district heating system shows growing interest [1,2]. However, solar energy resource are insufficient in the heating seasons but abundant in the non-heating seasons [2]. The mismatch between thermal energy demand and solar thermal production can be addressed using seasonal heat storage, resulting in higher utilization of solar energy [3]. Water is recognized as the best sensible heat storage material below 100 °C due to its low cost, high heat storage capacity, and environmental friendliness [4]. Therefore, water is widely used for different thermal energy storage techniques. Thermal stratification inside the storage is usually created by the buoyancy separation of hot and cold water inside the thermal storage, which significantly influences the thermal performance of solar heating systems [5–7].

Several heat transfer mechanisms can result in the loss or degradation of thermal stratification in thermal storage [8,9], for instance, thermal conduction in the storage due to the vertical temperature gradient, heat loss through the top insulation, and mixing at the inlet/outlet. Typically, the mixing effect is expected to occur in a small region near the inlet, but under unfavorable conditions, mixing may expand to the majority of the storage volume [10]. The leading cause of destratification, particularly for direct charge/discharge of thermal storage, is inlet mixing during the charge/discharge process [11].

Numerous experimental and numerical studies have been conducted to reduce inlet mixing. Some of them focused on creating correlations to guide the design of inlet configurations. For instance, a correlation for vertical inlet extraction efficiency based on the inlet Reynolds (Re) number, Grashof (Gr) number, and tank aspect ratio was established [12]. On that basis, the extraction efficiency for horizontal inlets was further adjusted [13]. Deng et al. [14] emphasized inlet configurations to where with water entering the thermal storage at a uniform low flow rate, favoring thermal stratification. In this context, inlet/outlet diffusers with baffle plates [14–18] and porous manifolds inlets [19–21] have been successfully suggested. Radial diffusers have recently been

* Corresponding author.
E-mail address: jifa@dtu.dk (J. Fan).

https://doi.org/10.1016/j.renene.2023.119170
Received 5 January 2023; Received in revised form 18 July 2023; Accepted 10 August 2023
Available online 11 August 2023

Nomenclature

Latin characters

a	Coefficient, [−]
b	Coefficient, [−]
CFD	Computational fluid dynamic, [−]
C_p	Specific capacity, [J/kg·K]
c	Coefficient, [−]
D	Diameter, [m]
F	Buoyancy flux, [m^4/s^3]
Fr	Froude number, [−]
Gr	Grashof number, [−]
g	Gravity, [m/s^2]
H	Distance between diffuser discs, [m]
M	Inlet momentum flux, [m^4/s^2]
m	Mass flow rate, [kg/h]
Re	Reynolds number, [−]
Ri	Richardson number, [−]
PTES	Pit thermal energy storage, [−]
T	Temperature, [^oC]
t	Time, [s]
V	Volume flow rate, [m^3/h]
v	Inlet velocity, [m/s]
Z	Penetration height, [m]

Subscripts

bottom	Bottom diffuser
d	Diffuser
h	Hydraulic diameter
in	Inlet
j	Number of layer in PTES
m	Mixed water
middle	Middle diffuser
out	Outlet
start	Energy starts to distribute in a layer
top	Top diffuser
0	Initial

Greek

ρ	Density, [kg/m^3]
μ	Dynamic viscosity, [kg/m·s]
η	Energy distribution ratio, [−]
θ	Dimensionless temperature, [−]

studied in detail using Computational Fluid Dynamic (CFD) and experiments by Findeisen et al. [22–26]. They emphasized that when there was a large distance between the diffuser and storage top wall, the stratification quality could be significantly reduced due to strong mixing. Therefore, they suggested mounting the diffuser on the top of the storage tank to improve the thermal stratification.

1.1. Modeling of inlet mixing

Computational modeling of heat transfer and fluid flow in solar heating systems provide a valuable tool for evaluation of system performance [27]. Therefore, mathematical models of thermal storage are developed for integration into the system's dynamic simulations. The commonly used models are mostly based on simplified one-dimension energy balance approaches. These approaches significantly reduce the model complexity but also mean that the detailed flow structures, especially the three-dimensional phenomena of inlet mixing, cannot be directly modeled.

In the early years, some researchers considered the mixing processes by introducing an eddy conductivity factor into the energy equation to compensate for the discrepancy in one-dimensional models. Oppel et al. [28] established a functional relation of inlet eddy conductivity factor for circular inlets and solid circular plate inlets using the *Re* number and Richardson (*Ri*) number. When used with a one-dimensional model, the obtained correlations gave good predictions of the thermocline development. Zurigat et al. [17,29] further characterized the turbulent mixing for various inlet configurations using the same methods. Those inlet configurations included side inlet, side inlet with perforated baffle, impingement inlet, solid diffuser, perforated diffuser, and perforated diffuser with a solid center. Their study showed that the effective diffusivity factor could be a practical measure for quantifying mixing effects introduced by different inlet configurations. Najem and Rafaee [30] also incorporated an eddy conductivity factor into their finite element model, which agreed with the experimental results.

In recent years, researchers have attempted to characterize the mixing effect by quantifying the mixing region geometry or mixing coefficient. The ratio of the sum of the mixing zone and the inflow heat capacities to the mixing zone heat capacity is known as the mixing coefficient. It was found that the mixing coefficient can be expressed as a function of *Re* and *Ri* numbers [31]. Further, Karim et al. [32] found that after the thermocline formation, the inlet flow velocity could be increased without increasing the inlet mixing. They adjusted the mixing coefficient versus inflow velocity when achieving a fully developed thermocline. Shah and Furbo [16] carried out both theoretical and experimental analysis to characterize the inlets impact on the thermal conditions. The findings indicated that the *Ri* number, tapped water volume percentage, temperature difference, and thermal expansion coefficient all impacted the changes in entropy and exergy during discharge. However, the limited amount of experimentally obtained data could not propose the correlation of these parameters. Further research by Jordan and Furbo [33] revealed that the inlet height could be defined as a function of the inlet mass flow rate and density difference in the storage tank. In this case, the degree of mixing under different operating conditions could be characterized in a one-dimensional model by changing the inlet position during the dynamic simulation. The simulated results of the storage temperature distribution were more consistent with the measured results when using a variable inlet height than when using a fixed inlet height.

Furthermore, Nizami et al. [27] developed a new one-dimensional model capable of considering the mixing characteristics created by vertical inflow. According to parametric CFD studies, jet penetration depth and entrainment mass flow rates were obtained as a function of the *Ri* number and inlet diameter. The temperature predictions of the new model were compared to the experimental results with good agreement. However, it could not easily be extrapolated to other inlet configurations. Most recently, a new one-dimension model for tank thermal storage was proposed by Brecht et al. [34]. The model included two parameters in the energy equations, mixing coefficient and mixing zone height. The mixing coefficient had a linear relationship with the *Re* number, and the mixing zone height was related to the inflow *Fr* number, inflow *Re* number, and the ratio of the inlet diameter to the tank diameter. The model demonstrated the significance of precisely modeling of the mixing effect generated by direct inflow in small-scale tank thermal storage, even with slight differences from the experimental results.

1.2. Motivation

According to the aforementioned literature, mixing may still occur under certain conditions, even with the proper inlet design. The one-

dimension models can be adjusted to improve the calculation accuracy by introducing the inlet mixing empirical correlations. However, all the reported methods incorporating the mixing effect are based on limited data from experiments or CFD simulations of small-scale thermal storage. In other words, the empirical relationships proposed in the studies can only apply to specific situations and may not be applicable to other heat storage, for example, large-scale water pit heat storage.

The commonly used one-dimensional models for PTES are Type 342, Type 343, Type UGST, as well as the newly developed models Type 1535 and Type 1536, which are built in the TRNSYS simulation software [3]. However, it is important to note that these existing models do not currently account for the phenomenon of the inlet mixing within PTES. For one thing, there is a lack of research on the influence of inlet mixing on PTES performance. Additionally, the mixing effect depends not only on the design of the PTES but also on its operating conditions [35], making it challenging to introduce the three-dimensional characteristics of inlet mixing into a one-dimensional model.

Therefore, it is crucial to fully understand the effect of inlet mixing on PTES performance and to develop a straightforward method to incorporate it into the one-dimensional model to improve its calculation accuracy.

1.3. Contribution and organization of the paper

To address the above-mentioned research gaps, this study aims to analyze the potential inlet mixing phenomenon in the context of the Dronninglund project's operational conditions. The primary focus is to develop a comprehensive understanding of the inlet mixing effect within the PTES, employing a full-scale three-dimensional CFD model.

The developed CFD model allows for the visualization of the inlet mixing phenomenon, providing insights into its dynamic behavior within the PTES. Various operating scenarios are simulated to thoroughly evaluate and quantify the impact of inlet mixing on PTES performance. In this instance, appreciate correlations are proposed to characterize the penetration height of the inlet mixing area and the energy distribution ratio for each layer.

The findings of the investigations will further contribute to understanding the inlet mixing phenomenon inside PTES and improving the calculation accuracy of one-dimensional models.

2. Experimental study

2.1. System overview

The Dronninglund solar district heating (SDH) plant has been demonstrated to be one of the most successful projects. The system can cover up to 70% of the heat demand using renewable energy [36]. A schematic diagram of the Dronninglund SDH system is shown in Fig. 1. The system's major components are two solar collector fields with a total aperture area of 35,573 m^2, a 60,000 m^3 pit thermal energy storage (PTES), and an absorption heat pump. During charging, the top of the PTES is heated by the heat from the outlet of the solar collector fields. Notably, the middle inlet/outlet (yellow line in Fig. 1) is used at certain times to help manage stratification within the PTES [37]. For instance, if the top of the PTES reaches 85 °C and the solar collector fluid is heated to 60 °C by the solar collector fields, the PTES is charged by the solar heat through the middle diffuser than the top diffuser. During discharge, when the PTES temperature is high enough, water is taken from the top of the PTES and used directly for the district heating grid. When the PTES temperature is too low for direct use, the heat pump extracts heat from the PTES, resulting in high storage efficiency [36]. In addition, the system is equipped with a combined heat and power plant fed by four gas engines, a bio-oil boiler, and a natural gas boiler to supply the remaining heat requirements [38].

It should be noted that due to the proper utilization of the PTES, the average solar fraction of the system can reach 40% in the past few years of operation. Therefore, this study will focus on understanding the dynamic behaviors of the PTES during charging and discharging. An aerial view of the Dronninglund PTES and its inner structure during construction is shown in Fig. 2.

2.2. The PTES design

Dronninglund PTES consists of the water body, the cover, the connection pipes, and the inlet/outlet diffusers as depicted in Fig. 3 (a). The water body is shaped like a regular quadrilateral pyramid with a base side length of 26 m, a top side length of 90 m, and a height of 16 m. A slope angle of 26.6° to is specially chosen for the water body to reduce construction costs and prevent sidewall collapse [38–41]. In addition, an insulating cover is installed to seal the water body, and a waterproof liner is applied to the sides and the bottom surface of the PTES to isolate the water from the surrounding soil.

PTES is typically designed large enough to accommodate long-term storage needs. Three diffusers are installed at the top, the middle, and the bottom of the PTES, respectively. The top diffuser is close to the top of the PTES, while the bottom diffuser is near the bottom of the PTES. Each diffuser is equipped with two radial discs. These designs help maintain thermal stratification by introducing water enters PTES at a uniform and slow rate at various temperatures [16,18]. Fig. 3 (b) illustrates the detailed design of the Dronninglund PTES inlet.

2.3. The measurements and uncertainties

In order to monitor the PTES's behavior, several sensors have been mounted in and around the PTES [36,37]. The different types of sensors used in this study and their locations are described as follows:

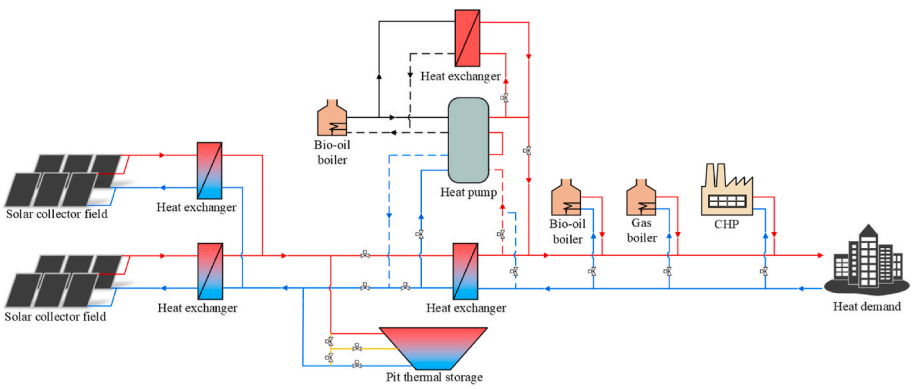

Fig. 1. A simplified schematic of the Dronninglund solar district heating plant.

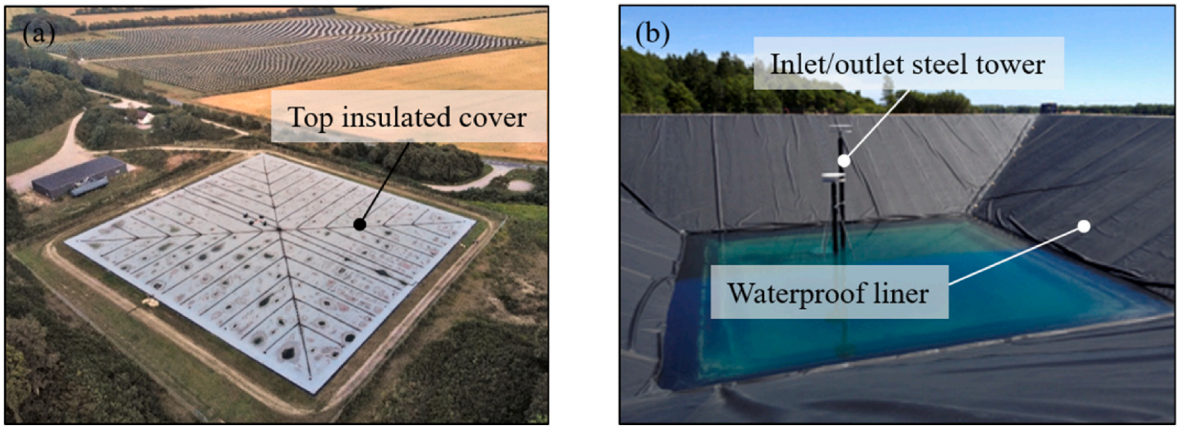

Fig. 2. Photo of Dronninglund PTES: (a) Aerial view (2019) [7], (b) Inner structure (Image source: PlanEnergi).

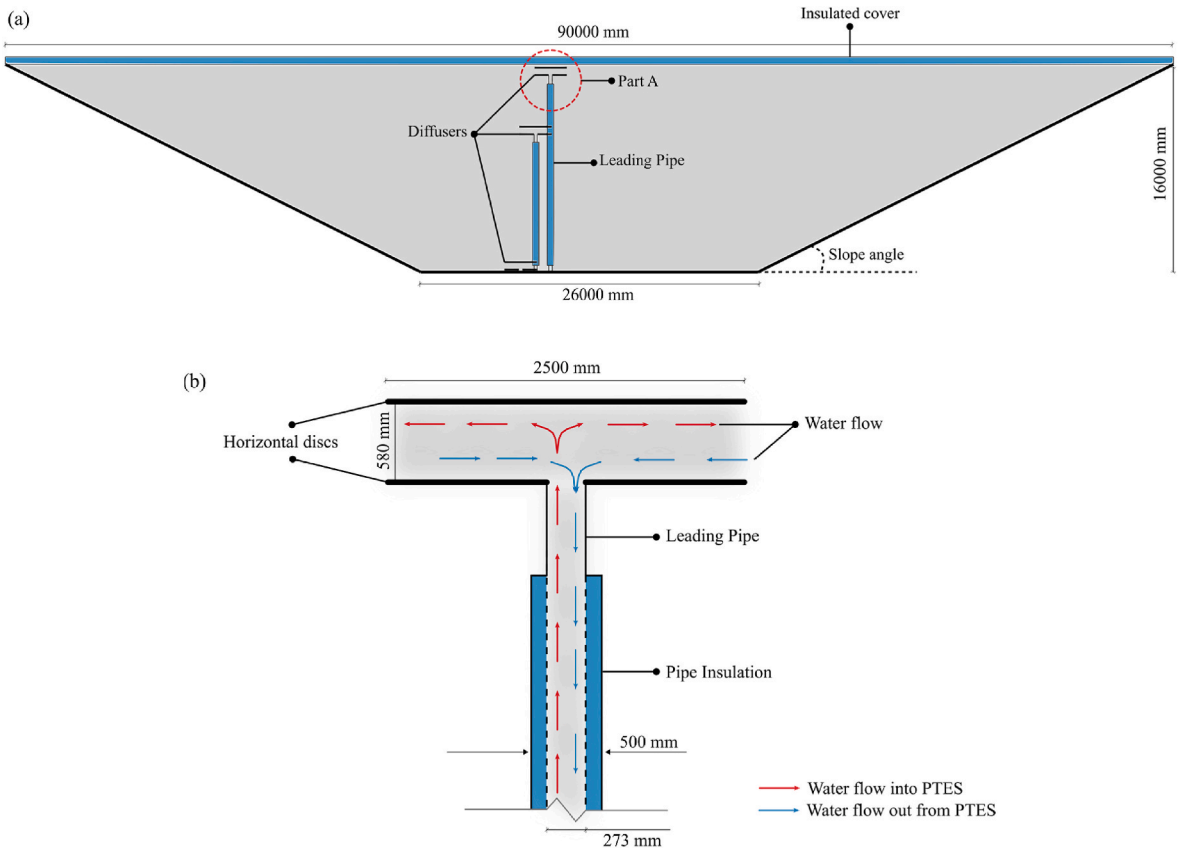

Fig. 3. Schematic of the Dronninglund PTES: (a) Main design of the PTES, (b) Enlarged view of Part A (inlet detailed dimensions), the red vectors indicate the flow when the diffuser is used as an inlet, the blue vectors indicate the flow when the diffuser is used as an outlet. (For interpretation of the references to colour in this figure legend, the reader is referred to the web version of this article.)

1) There are 32 temperature sensors installed inside the PTES, one of which is located 0.1 m below the insulating cover, and the other 31 are spaced 0.5 m from the bottom to the top of the PTES.
2) Two temperature sensors are placed on the top and the bottom surface of the insulating layer, respectively.
3) Three temperature sensors and three flow meters are installed in the pipes (sections in the technical building) connected to the three diffusers. It is worth mentioning that the flow meters measure both direction and flow rate.

The temperature sensors are Class A PT100, with an accuracy of ±0.15 K [7]. Electromagnetic flow meters are used to measure the volume flow rate, and their accuracy is 0.4%. All the measurements are recorded at 10-min intervals.

2.4. The operation of the PTES

The Dronninglund PTES serves as long-term and short-term heat storage to balance the heat production by the solar collector fields and the heat demand of the district heating consumers. Water is used as the storage material, which means it will naturally stratify due to the density difference between hot and cold water [42]. It is important to note that inlet mixing caused by high inlet flow rates or large temperature differences between the incoming water and the water in the PTES may

significantly contribute to the destruction of thermal stratification [43, 44]. In this case, appropriate operating strategies should be selected to minimize mixing during the charge and discharge of the heat storage.

In practice, the operation of the inlet/outlet diffuser is complicated as it depends on the supply temperature from the solar collector field, the heat demand of the district heating network, and the PTES temperatures. Table 1 summarizes the inlet/outlet diffusers combinations of the PTES based on the measurements in 2017, where '1' means the diffuser operates as an outlet, '0' means the diffuser operates as an inlet, and '/' means on standby. As observed, the bottom diffuser is used as an inlet for most of the year. The top or the middle diffuser serves as an inlet in approximately 15% of the year.

In order to identify typical operation conditions for the investigations of inlet mixing, Fig. 4 shows the inlet temperatures, inlet volume flow rates, and the PTES temperatures at the levels of the inlet diffusers.

The top diffuser operates mainly from March to August, with a volume flow range of 0–400 m^3/h. At certain times in March, July, and August, the inlet volume flow rate occasionally reaches 500 m^3/h. The inlet temperature is always higher than the PTES temperature at the level of the top diffuser, with a maximum temperature difference of over 60 K in March. However, in April and August, the inlet temperature is sometimes lower than the PTES temperature at the level of the top diffuser.

The middle diffuser operates mainly from March to August, but the inlet flow rate is lower than that of the top inlet. The volume flow rate typically varies between 0 and 250 m^3/h. The maximum volume flow rate is around 300 m^3/h. From April to July, the inlet temperature is higher than the PTES temperature at the level of the middle diffuser, with a maximum temperature difference of 50 K. Most of the time, lower-temperature water with a maximum temperature difference of −30 K is introduced into PTES from August to March.

Except for May, the bottom diffuser operates as an inlet most of the year with a flow rate below 100 m^3/h. In addition, the inlet temperature is the same as the PTES temperature at the level of the bottom diffuser most of the time. Notably, there are periods from March to May when the inlet temperature is higher than the PTES temperature at the level of the bottom diffuser. The most noticeable temperature difference is around 10 K.

In conclusion, the inlet temperature may not always be the same as the PTES temperature at the level of the inlet diffuser due to the fixed position of the inlet/outlet diffusers. In this situation, even with the radial diffuser being used as the inlet stratification device, inlet mixing may still occur in a certain region within the PTES, especially when there is a notable temperature difference between the inlet and the PTES.

Table 1
The inlet/outlet diffusers combinations of the PTES in the year 2017.

Flow path no.	Direction			Operation percentage
	Top	Middle	Bottom	
1	0	1	1	8.0%
2	0	0	1	2.9%
3	0	/	1	2.3%
4	0	1	0	4.2%
5	1	0	0	5.2%
6	1	0	1	3.9%
7	1	1	0	35.2%
8	1	/	0	27.6%
9	1	0	/	2.8%
10	/	0	1	1.2%
11	/	1	0	1.9%
12	/	/	/	4.8%

3. Numerical study

3.1. Model description

Based on the PTES size of the Dronninglund project described in Section 2.2, a full-scale three-dimensional model was developed in ANSYS. The model includes both the water and the soil region, as shown in Fig. 5 (a). It should be noted that the soil region is created large enough to minimize the impact of soil boundaries on changes in soil temperature near the water body. The water region was considered an incompressible fluid with temperature-dependent thermophysical properties, while the soil region was treated as a solid region with constant thermal properties.

Reynolds-average transport equations were solved by ANSYS FLUENT for flow and energy fields using the realizable k-ϵ model to accurately reflect the inlet mixing process caused by inflow and outflow [45]. After a mesh study of 0.5, 0.7, 0.9, and 1.6 million cells, the numerical mesh with a density of 0.9 million cells was found to be a good compromise between accuracy and calculation time. The readers are recommended to refer to the literature [46] for more information on the developed CFD model, inclusive of the geometry, the mathematical method, the mesh, and the numerical procedure.

3.2. Boundary conditions

The CFD model has been successfully verified using short-term operational measurements of the Dronninglund PTES [46]. However, it was observed that the case on June 2 had a lower PTES temperature calculation accuracy than the other cases. The discrepancy can be attributed to a considerable temperature gradient in the top of the PTES [46]. In this context, this validation focused on the period from June 1 to June 7 to further demonstrate the model's long-term reliability for accurately assessing the inlet mixing phenomenon.

As the boundary condition of the long-term validation, Fig. 6 presents the operational conditions from June 1 to 7. The initial temperature distribution inside PTES is shown in Fig. 6 (a), with a uniform temperature of 36 °C below 13 m and a significant temperature gradient of 22 K/m exists between 13.5 m and 15.5 m. During this time, hot water primarily enters from the top diffuser to charge PTES at daytime, while cold water enters from the bottom diffuser to discharge PTES at night. Additionally, hot water enters from the middle diffuser to charge PTES when the water temperature from the solar collector field is lower than that of the PTES top.

3.3. Long-term validation

3.3.1. Water temperature

Fig. 7 compares the Dronninglund measurements with the calculated PTES temperature using the CFD model at a 10-min resolution. The measured temperatures were readings of the temperature sensors at different heights, while the calculated temperatures were taken from the CFD model at the corresponding heights. The PTES temperatures from the bottom to the top at 0:00 from June 1 to June 8 are depicted in Fig. 7 (a). It is evident that there is a good agreement between the calculated and measured temperatures. However, a significant temperature difference of 6 K is observed at 14.5 m. Due to the large temperature gradient between 14 m and 15 m, the uncertainty in the sensors' position along the PTES height has a great impact on the reported PTES temperature [46]. To further illustrate this effect, Fig. 7 (b) includes the calculated temperature at 14.4 m, in addition to the measured and calculated temperatures at 14.5 m. The results demonstrate that accounting for sensor vertical movement uncertainty reduces the temperature difference between the calculated and the measured values.

3.3.2. Operation conditions

Fig. 8 illustrates the variation in inlet/outlet temperature and mass

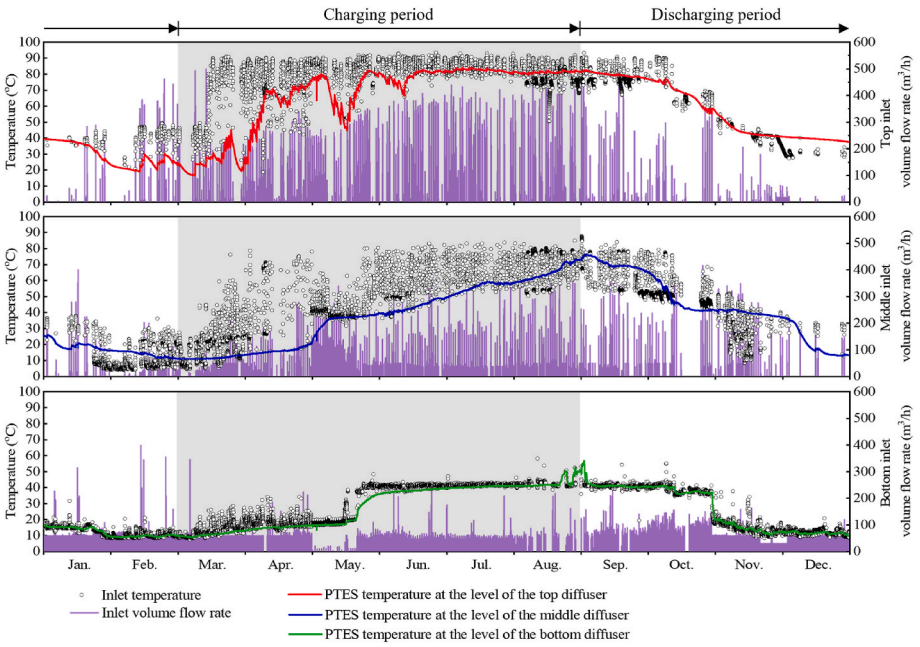

Fig. 4. Inlet volume flow rates, inlet temperatures and the PTES temperature at the levels of the inlet diffusers in 2017.

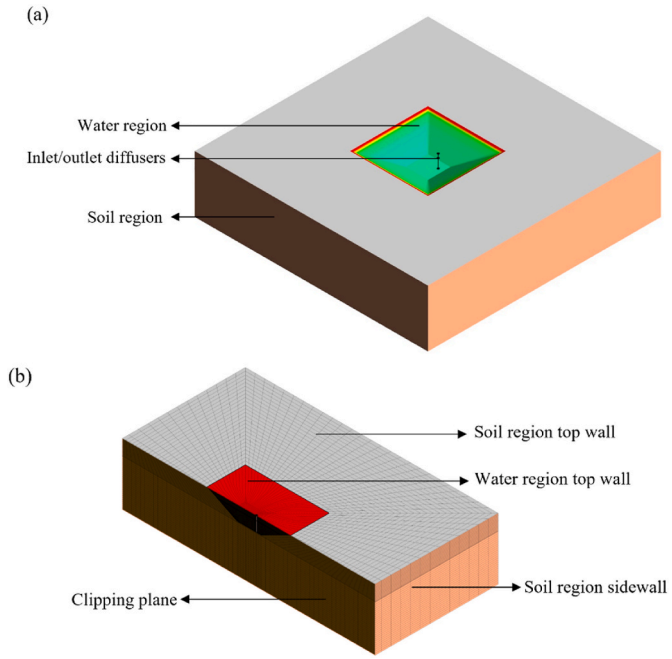

Fig. 5. Three-dimensional CFD model: (a) Model diagram; (b) Grid scheme (the clipping plane is positioned through the center of the diffusers to show the mesh inside the model).

flow rate variation from June 1 to June 7. There is qualitative agreement for the inlet/outlet operating conditions in terms of temperature and mass flow rate. The most significant deviation occurs when the top diffuser is used as the outlet. In theory, the outlet temperature should fall between the water temperatures at 15.12 m and 15.7 m, where the top diffuser is located. However, as mentioned earlier, there is considerable uncertainty in the actual temperature distribution between 14.5 m and 15.5 m due to the large temperature gradient. Therefore, the difference between the calculated and the measured results regarding the top outlet temperature is acceptable.

It is worth mentioning that this study focuses on developing the inlet mixing correlations. As a result, the calculated temperatures of the soil region have not been presented in this section since they do not play a significant role in the inlet mixing investigation. Overall, the agreement observed in PTES temperature distribution and inlet/outlet parameters suggests that the model can be confidently used to correlate the inlet mixing parameters.

4. Numerical study scenarios and parameters

4.1. Numerical study scenarios

4.1.1. Positive buoyancy effect

Based on the operation of the PTES in 2017, twelve case studies were determined and used to investigate the impact of positive buoyant jet mixing. In all simulations, the bottom diffuser was used as the inlet, and the top diffuser served as the outlet. The bottom diffuser is far from the PTES top wall and provides enough space for the diffusion of the buoyant jet. In this case, more features of positively buoyant jet can be found in different situations. The initial temperature (T_0) was uniformly 10 °C for all cases, while the inflow temperature (T_{in}), the inlet flow rate (V_{in}), the diameter of the diffuser disc (D_d), and the distance between the diffuser discs (H_d) were varied. Key parameters of the 12 cases are presented in Table 2, with the referred case highlighted in red background and the parameter variations based on the reference case highlighted in blue background. The monitoring data indicated that the operation conditions changed every 10-min, so the simulations ran for 10-min. Additionally, the simulation results were recorded every 10 s to fully characterize the transient behavior of the inlet mixture.

4.1.2. Negatively buoyant effect

Similar to the positive buoyant effect study, a series of 12 cases were performed to investigate the mixing effect of negative buoyant jets. The bottom diffuser was employed as the outlet, while the middle diffuser was used as the inlet for two reasons: (1) When the middle diffuser is used as the inlet, the inflow temperature is lower than the PTES temperature at the level of the diffuser for more periods than the top diffuser operates. (2) There is enough space for the jet flow to develop. In addition, the initial temperature (T_0) was uniformly 70 °C in the PTES, as shown in Table 3. Other simulation settings regarding simulation time and data sampling interval are the same as in Section 4.1.1.

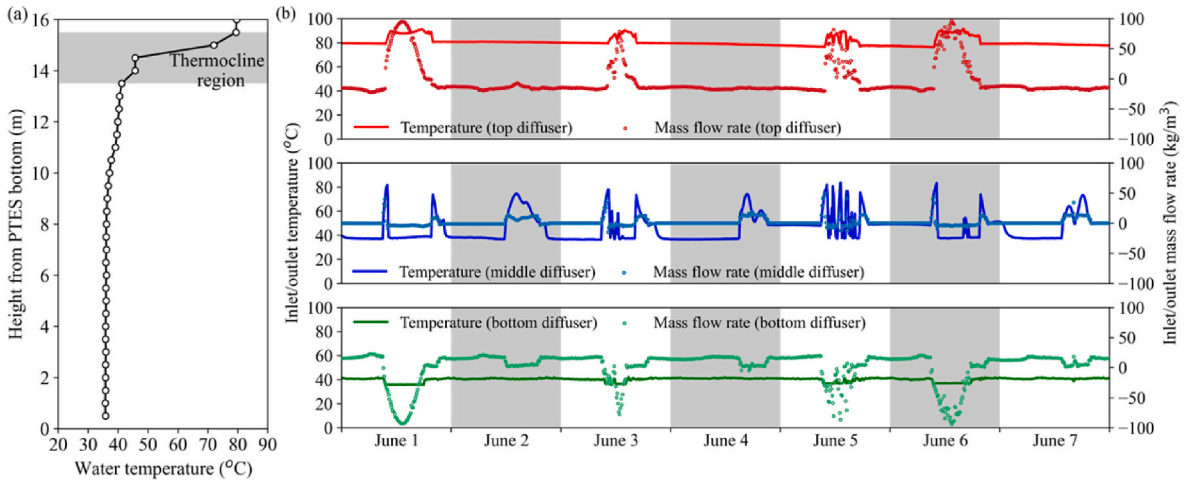

Fig. 6. Operational conditions during the validation period: (a) Initial PTES temperature distribution; (b) Inlet/outlet conditions (Positive flow rate: water enters the PTES; Negative flow rate: water flows out from the PTES).

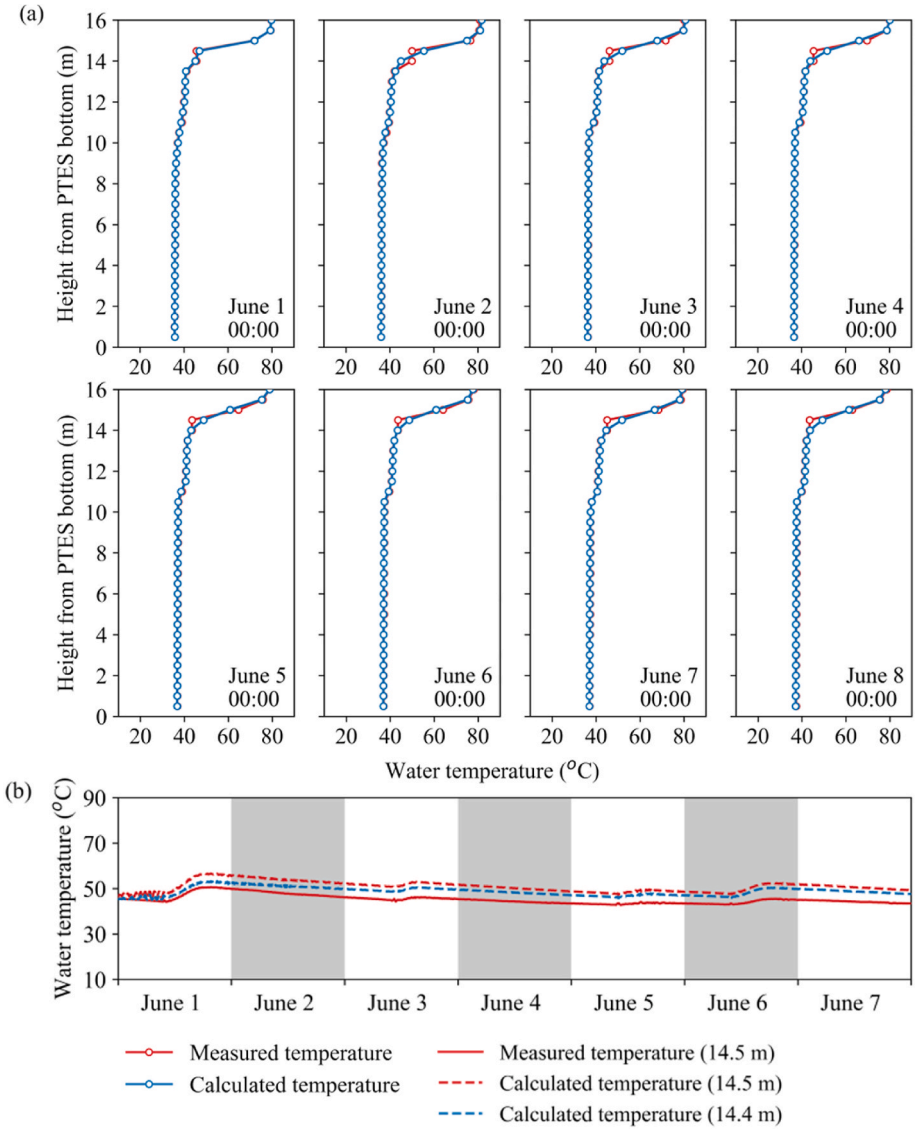

Fig. 7. Comparison of the measured and calculated PTES temperature from June 1 to June 7, 2017.

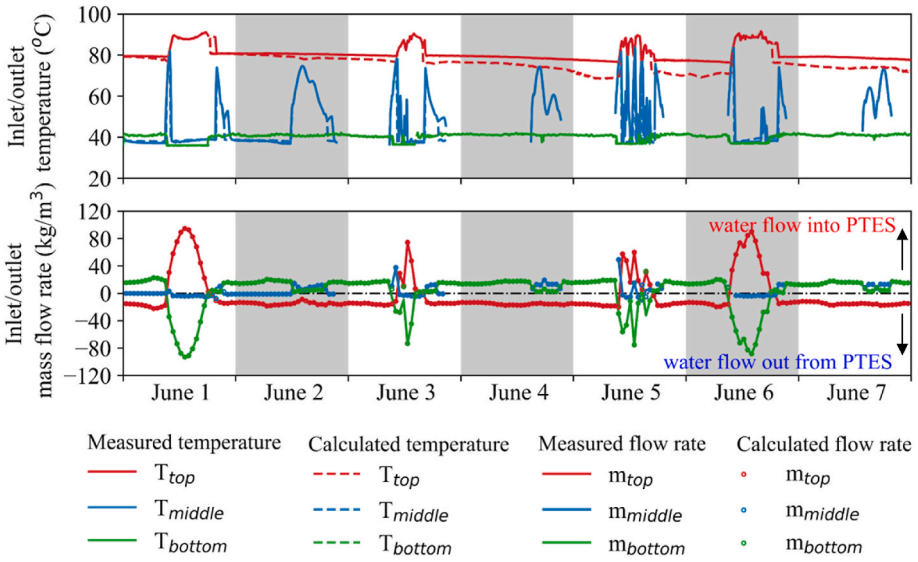

Fig. 8. Comparison of the measured and calculated inlet/outlet parameters from June 1 to June 7, 2017.

Table 2
Key parameters used in the investigations of positive buoyancy effect.

Case	Initial PTES temperature (T_0 (°C))	Inflow temperature (T_{in} (°C))	Inlet flow rate (V_{in} (m^3/h))	Diameter of diffuser disc (D_d (m))	Distance between diffuser discs (H_d (m))
1	10	20	10	2.5	0.58
2	10	20	50	2.5	0.58
3	10	20	100	2.5	0.58
4	10	12	50	2.5	0.58
5	10	30	50	2.5	0.58
6	10	40	50	2.5	0.58
7	10	20	50	0.5	0.58
8	10	20	50	1.5	0.58
9	10	20	50	3.5	0.58
10	10	20	50	2.5	0.48
11	10	20	50	2.5	0.68
12	10	20	50	2.5	0.78

Table 3
Key parameters used in the investigations of negative buoyancy effect.

Case	Initial PTES temperature (T_0 (°C))	Inflow temperature (T_{in} (°C))	Inflow rate (V_{in} (m^3/h))	Diameter of diffuser discs (D_d (m))	Distance between diffuser discs (H_d (m))
1	70	60	10	2.5	0.58
2	70	60	50	2.5	0.58
3	70	60	150	2.5	0.58
4	70	60	250	2.5	0.58
5	70	50	50	2.5	0.58
6	70	69	50	2.5	0.58
7	70	60	50	0.5	0.58
8	70	60	50	1.5	0.58
9	70	60	50	3.5	0.58
10	70	60	50	2.5	0.48
11	70	60	50	2.5	0.68
12	70	60	50	2.5	0.78

4.2. Performance index

To effectively quantify the inlet mixing impact, two parameters are introduced: the penetration height (Z) and the energy distribution ratio (η_j). These parameters aim to capture the changes in the affected areas and energy distribution variation resulting from inflow mixing under different scenarios.

4.2.1. The penetration height

Z represents the maximum height at which the inflow can affect, as illustrated shown in Fig. 9. It measures the difference between the maximum height of the mixing area and the height of the inlet position. In this study, Z is determined based on the CFD calculations. A dimensionless temperature represented in Eq. (1) is used as the metric to determine whether a point in the PTES is affected by the inlet flow.

$$\theta = \frac{T_t - T_0}{T_{in} - T_0} \tag{1}$$

Where T_{in} is the inflow temperature, T_0 is the PTES initial temperature, and T_t is the PTES temperature at time t. $\theta = 1$ means that a point in the PTES is completely replaced by inflow water, while $\theta = 0$ means that a point in the PTES is not affected by inlet flow. In this context, the larger the θ, the greater the temperature change at a certain location of the PTES caused by the inlet flow. Conversely, the smaller the θ, the smaller the temperature change at a specific position inside the PTES.

4.2.2. Energy change efficiency

Considering that the objective of this study is to quantify the degree of cross-layer mixing caused by fluid entrainment in the buoyant jet, the PTES was divided into 32 layers along the height, as shown in Fig. 9. Then, the energy distribution ratio of a layer is defined as follows:

$$\eta_j = \frac{\sum_0^t C_{p,jm} m_{jm,t} \left(T_{jm,t} - T_{jm,0}\right)}{\int_0^t m C_p (T_{in} - T_{out}) dt} \tag{2}$$

Where the numerator represents the energy stored in layer j and the denominator is the energy supplied to the entire PTES during the charge/discharge. $m_{jm,t}$ is the mixed water mass in layer j, and its specific heat is $C_{p,jm}$. $T_{jm,0}$ and $T_{jm,t}$ denote the initial temperature of the mixed water in the layer j and the temperature at time t, respectively. An energy distribution ratio of 1 for a layer means all the charged/discharged heat enters the layer, while an energy distribution ratio of 0 means the layer is not affected by the inlet flow. If the charged/discharged heat is evenly distributed over the 32 layers, the distribution ratio will be 1/32 for all layers. It is possible to determine the energy stored in each layer inside PTES resulting from inflow mixing based on the CFD simulations.

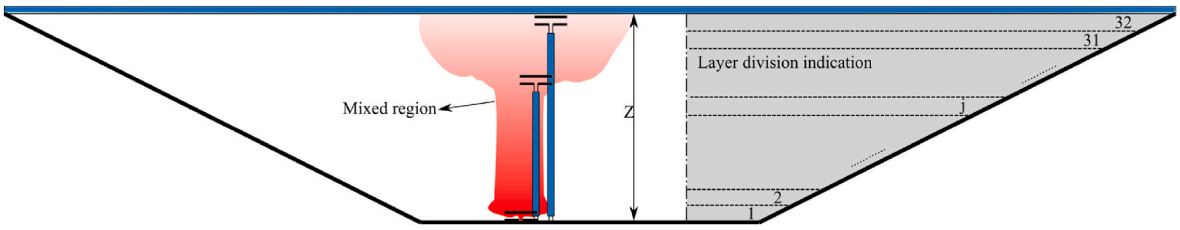

Fig. 9. Illustration of the mixed region in the PTES (The grey background illustrates the layer division in this study).

4.3. Dimensionless parameters

To obtain quantitative results for the inlet mixing effect, it is essential to establish a relationship with specific PTES characteristics. The characteristics of the PTES depend on the geometric configuration and operating conditions. The diffuser position and geometry are among the geometrical parameters. The inflow rate and the temperature difference between the incoming and resident water are the operating factors that are the most important.

4.3.1. Reynolds and Froude number

Dimensionless parameters are of great significance in the design and performance evaluation of stratified thermal storage and are used as indexes to evaluate the performance of stratified thermal storage [8,34,47,48]. Two dimensionless parameters are selected in this study to characterize the inflow forces and inertial forces. The inlet *Re* and *Fr* numbers are expressed as Eq. (3) and Eq. (4), respectively.

$$Re = \rho_{in} v D_h / \mu \tag{3}$$

$$Fr = v^2 \Big/ \left(D_h g \left(\frac{\rho_{in}}{\rho_0} - 1 \right) \right) \tag{4}$$

Where ρ_{in} and ρ_0 represent the inflow temperature and the PTES initial temperature, respectively. v is the average inflow velocity, μ is the kinematic viscosity, and g is the acceleration of gravity. $D_h = \frac{4\pi D_d H_d}{\pi D_d + H_d}$ is the characteristic length that is used instead of the inlet pipe diameter because the buoyant jet formation is also related to the diffuser geometry (with detailed analysis in Section 5).

4.3.2. Momentum and buoyancy flux

Inspired by previous studies, the mixing flow depends on the momentum M and the buoyancy flux F when the inlet diameter is small compared to the jet penetration height. In this case, it is expected that M and F can be used to determine the inlet mixing impact. The following equations give the expressions for momentum M and the buoyancy flux F:

$$M = \pi D_h^2 v^2 \tag{5}$$

$$F = \pi \left[\frac{g(\rho_{in} - \rho_0)}{\rho_0} \right] D_h^2 v \tag{6}$$

M characterizes the inertia force of the inlet flow while F describes the buoyancy force of the inlet flow. It is important to note that in the following sections, *Fr* and F are expressed in their absolute values to harmonize the format of buoyancy in positive and negative buoyancy jets.

4.3.3. Dimensionless penetration height and time

In the context of inlet mixing, it has been demonstrated that all inflow properties can be scaled in terms of combination of M and $|F|$. The penetration height (Z) should be scaled as the dimensionless penetration height ($Z \bullet M^{-3/4} \bullet |F|^{1/2}$) [49,50]. The time ($t$) should be scaled as the dimensionless time $t|F|/M$ [51]. These scaling relationships allow for a more generalized representation of the penetration height and the temporal evolution of the inlet mixing, considering the combined effects of the inflow momentum and buoyancy flux.

In summary, the mentioned indexes provide a framework for analyzing and comparing the inlet mixing behavior in a dimensionless manner. In particular, it makes it possible to quantify the inlet mixing effect across different cases, facilitating the evaluation of inlet mixing degree. Section 5 will present the correlations of these parameters for various cases.

5. Results

5.1. Physical nature

5.1.1. Positive buoyant effect

The development of a positive buoyant jet and the energy distribution ratio along the PTES height at the specific time (left) are shown in Fig. 10. Note that the red curve in the energy distribution ratio diagram indicates the actual energy distribution ratio in the 32 layers. In comparison, the blue curve in the diagram represents that the delivered energy is evenly distributed among the 32 layers inside the PTES.

Initially, water enters the diffuser and reaches the upper diffuser disc. The jet starts to spread radially but remains concentrated near the inlet diffuser in the first 20s. Most of the energy provided is distributed near the bottom diffuser. The water flow starts to rise when it reaches the disc's outer edge, driven by the buoyancy force. Over time, the penetration height is getting larger, as well as the region of influence. The penetration height reaches the middle diffuser in around 300s. At the same time, the energy distribution ratio significantly changed, with more energy being distributed between 6 and 8 m inside PTES. At the end of the calculation, the jet reaches the top of the PTES, and part of the water flows downward, forming a recirculation region. More water is induced and brought to the top of the PTES, resulting in a larger distribution ratio.

5.1.2. Negative buoyant effect

Flow visualization of the transient behavior of a negatively buoyant jet is shown in Fig. 11, where Z is the downward penetration height, and $Z^{'}$ is the upward penetration height.

The jet flow reaches the upper diffuser disc in a short time, which weakens the upward momentum and changes the flow direction (20 s). During this period, the influenced area is confined near the middle diffuser. Then, driven by the negative buoyancy force, the water flows downward. As time progresses, the mixing region expands downwards, and the jet becomes noticeably asymmetric. The jet reaches the bottom of the PTES in about 300s. Additionally, it is evident that the location of the maximum energy distribution ratio shifts from the layers near the middle entrance to the layers of PTES bottom within the first 300s. Furthermore, it spreads radially until it reaches the PTES sidewall (t = 600s). Notably, the upward penetration height $Z^{'}$ is limited within the distance between the diffuser discs, since the upper diffuser disc blocks its upward path.

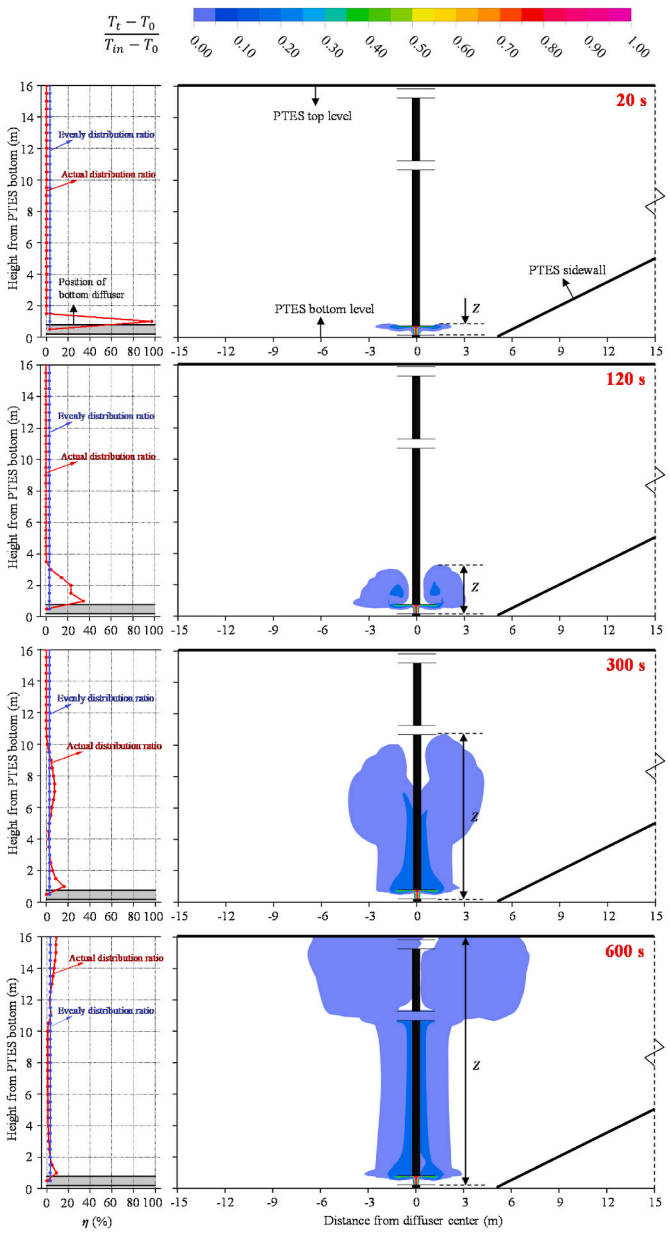

Fig. 10. Flow visualization of a positive buoyant jet. Based on Case2, with T_0 = 10 °C, T_{in} = 20 °C, V_{in} = 50 m^3/h, D_d = 2.5 m and H_d = 0.58 m.

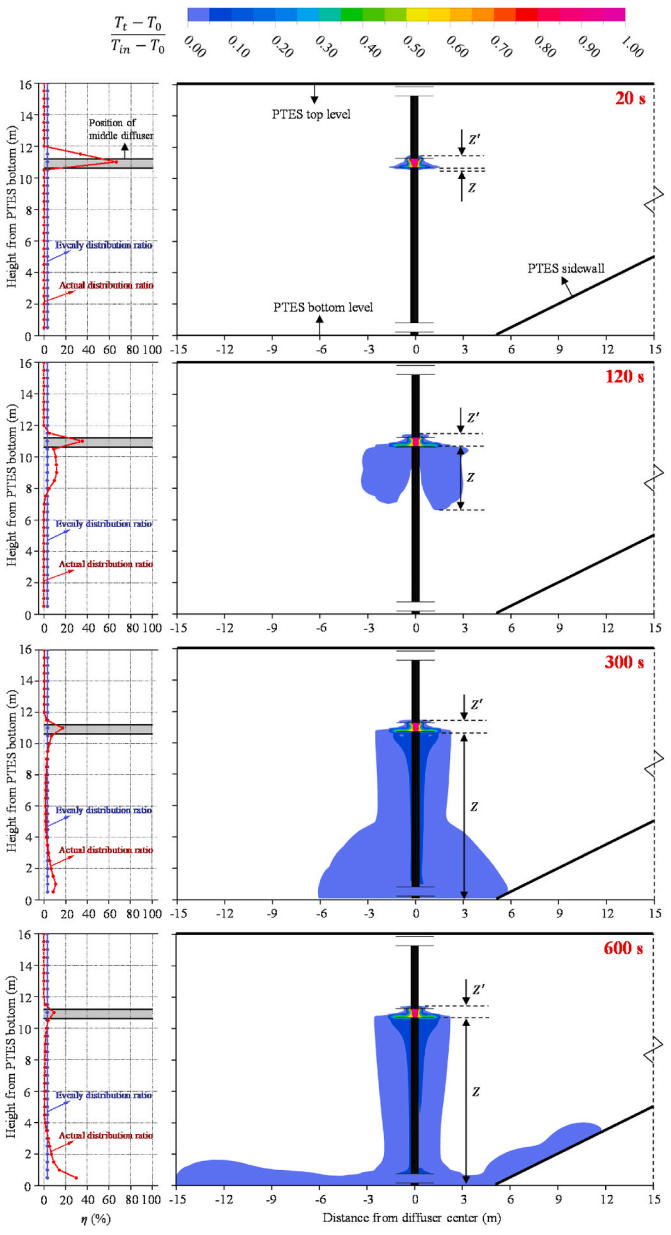

Fig. 11. Flow visualization of a negative buoyant jet. Based on Case2, with T_0 = 70 °C, T_{in} = 60 °C, V_{in} = 50 m^3/h, D_d = 2.5 m and H_d = 0.58 m.

5.2. Parametric analysis of penetration height

5.2.1. Positive buoyant jet

The inflow rate (V_{in}), the temperature difference (ΔT) between the inflow and the PTES, and the diffuser size (D_d and H_d) affect the extent of the inflow mixing zone. Fig. 12 displays the time history of the penetration height for a positive buoyant jet under different conditions. The solid and dash lines represent the positions of the upper and lower discs of the bottom diffuser, respectively. Changes of V_{in}, D_d and H_d contribute to the change of the *Re* number, while change of ΔT contributes to the change of the *Fr* number.

The upward momentum of jet will be increased for positive buoyancy where the momentum and buoyancy are in the same direction. The inlet flow reaches PTES top in less than 600s, except for cases with an inflow rate of 10 m^3/h and a temperature difference of 2 K. In addition, the penetration to the top of the PTES occurs faster for higher *Re* numbers because of a larger jet momentum. A larger *Fr* number can also cause the jet to reach the PTES top faster due to greater buoyancy. Moreover, H_d does not significantly affect penetration since the disc distance varies very little to ensure that the diffuser distributes the inflow effectively.

Based on the dimensional theory, the relation between the dimensionless penetration height and time for a positive buoyant jet is shown in Fig. 13. The inlet *Re* number falls in the range of $1292 \leq Re \leq 25348$ and the *Fr* number in the range of $6.5 \times 10^{-6} \leq |Fr| \leq 5.2 \times 10^{-3}$. A power-law relation between the dimensionless height and the dimensionless time is found for all the investigated cases. However, the coefficients fitted for the *Re* number of 1292 differ from those of the rest, as shown in Eq. (7). The different behavior of the inlet flow with a *Re* number of 1292 could be explained by its low inlet flow rate. As shown in Eq. (5) and Eq. (6), the influence of the inlet velocity on momentum is much greater than that of the buoyancy.

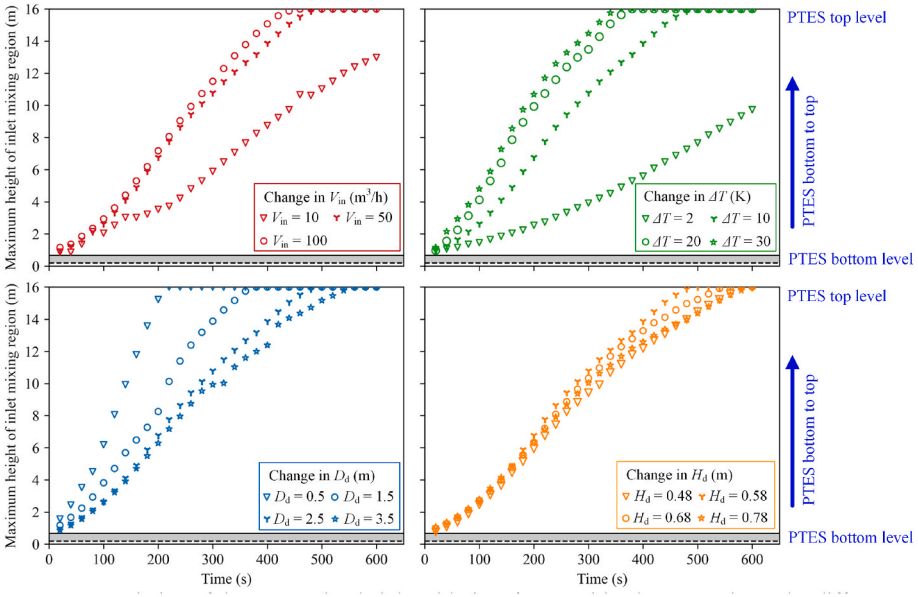

Fig. 12. Variation of the penetration height with time for a positive buoyancy jet under different operation conditions.

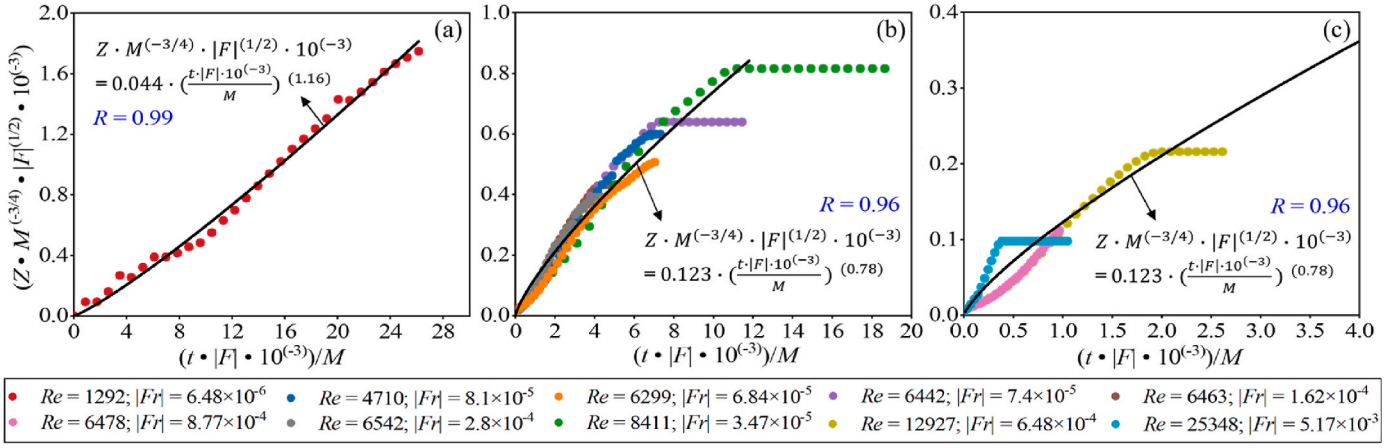

Fig. 13. Relationship between the dimensionless penetration height and time for a positive buoyant jet.

$$Z \bullet M^{\left(-\frac{3}{4}\right)} \bullet |F|^{\left(\frac{1}{2}\right)} \bullet 10^{(-3)} = \begin{cases} 0.044 \bullet \left(\dfrac{t \bullet |F| \bullet 10^{(-3)}}{M}\right)^{1.16} & Re \le 1292 \\ 0.123 \bullet \left(\dfrac{t \bullet |F| \bullet 10^{(-3)}}{M}\right)^{0.78} & Re > 1292 \end{cases} \quad (7)$$

In conclusion, Eq. (7) can be used to predict the penetration height of a positive buoyancy jet during operation, but attention should be paid to the applicable range of the inlet *Re* number.

5.2.2. Negative buoyant jet

Fig. 14 display the penetration height over 600s for each case given in Table 3. The solid and dash lines represent the positions of the upper and lower discs of the middle diffuser, respectively.

The largest upward penetration height ($Z^{'}$) can be reached more quickly by water at a higher inlet volume flow rate (V_{in}), but for a smaller V_{in} of 10 m^3/h, it takes around 100s to reach the maximum $Z^{'}$. For a more significant temperature difference (ΔT), $Z^{'}$ stabilizes earlier, while buoyancy takes longer to offset the effect of momentum at smaller ΔT.

When V_{in} and ΔT are increased, the penetration to the PTES bottom occurs more quickly, and the downward penetration height (Z) increases faster. Besides, lowering D_d results in a more considerable *Re* number, which can also speed up the increase of Z. However, the inlet *Re* value changes by 1% for every 0.1 m increase in H_d. In this case, it affects the penetration height slightly.

However, the maximum upward penetration height $Z^{'}$ for all the cases are limited is only about 0.3 m above the middle diffuser upper disc, and there is no great tendency to spread radially within the diffuser region. Therefore, we assume that the mixing above the inlet is negligible when the flow enters with a temperature lower than that of the PTES at the level of the diffuser.

In this context, only the relationship between the downward penetration height Z and time is established based on the dimensional theory for the negative buoyancy jet. The relationship between the dimensionless time and penetration height is illustrated in Fig. 15. Both the solid curves show a power-law fit, but they differ in terms of *Re*. The curve in Fig. 15 (a) needs to be considered when the *Re* number is less than 1272, while the curve in Fig. 15 (b) and (c) is considered when the *Re* number is higher than 1272. As a result, the prediction of the penetration height should follow Eq. (8) as specified in this study.

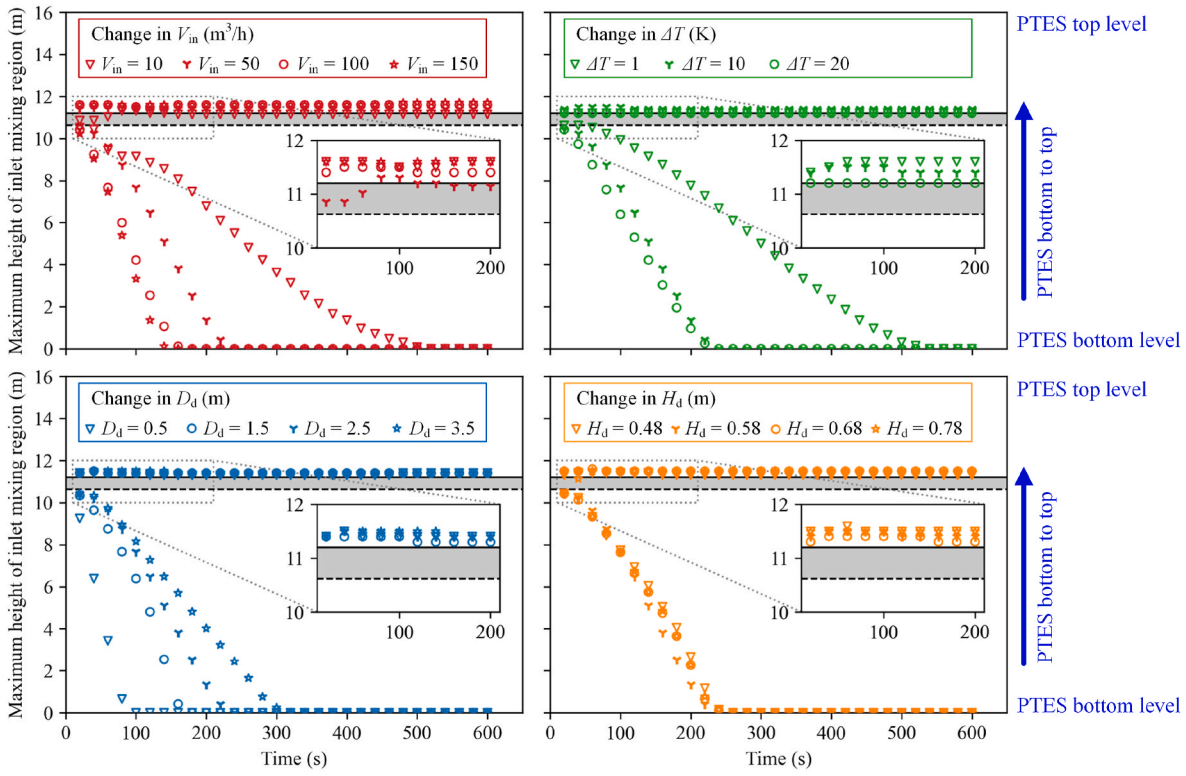

Fig. 14. Variation of the penetration height with time under different operation conditions for a negative buoyancy jet.

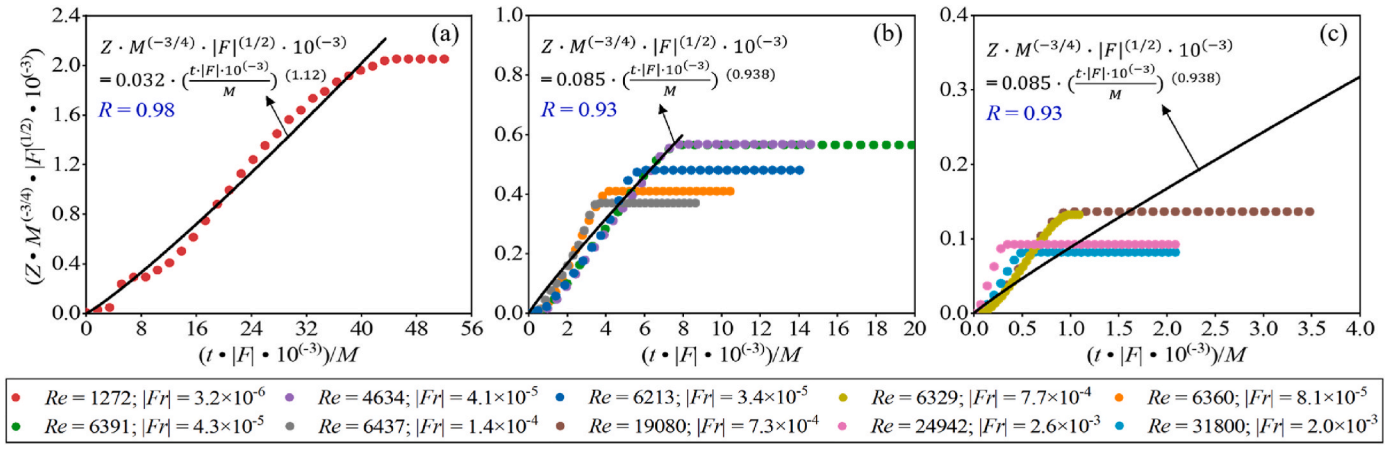

Fig. 15. Relationship between the dimensionless penetration height and time for a negative buoyant jet.

$$Z \bullet M^{\left(-\frac{3}{4}\right)} \bullet |F|^{\left(\frac{1}{2}\right)} \bullet 10^{(-3)} = \begin{cases} 0.032 \bullet \left(\dfrac{t \bullet |F| \bullet 10^{(-3)}}{M}\right)^{1.12} & Re \le 1272 \\ 0.085 \bullet \left(\dfrac{t \bullet |F| \bullet 10^{(-3)}}{M}\right)^{0.938} & Re > 1272 \end{cases} \tag{8}$$

5.3. The energy distribution ratio

5.3.1. Positive buoyant jet

Fig. 16 represents selected cases where there is a significant difference between the energy distribution ratio (η_j) of the layers inside the PTES. The circles are colored according to the value of the ratio. Smaller circles represent a smaller energy distribution ratio, while larger circles represent a more significant energy distribution ratio. It shows that the layer above the bottom inlet (i.e., the second layer) always has a large energy distribution ratio in the first 100s of the calculation because the inlet water continuously accumulates in this layer before being dispersed. Over time, the energy distribution ratio of the second layer decreases gradually and varies depending on the conditions. In addition, as more and more mixed water enters the top layer, the energy distribution ratio of the 32nd layer increases. Moreover, for the other layers inside the PTES, the energy distribution ratio is less than 10% during the calculation.

For comparison, we briefly describe the results for two cases. In Case 1, when V_{in} is reduced to 10 m^3/h, the large energy distribution ratio is obviously concentrated in the layers near the bottom inlet, while the upper layers of PTES are hardly affected. This is because it is challenging for the buoyancy jet to penetrate the top layers with small momentum during the calculation. The inlet momentum and buoyancy are significantly increased for Case 7 when D_d is reduced to 0.5 m. As a result, the

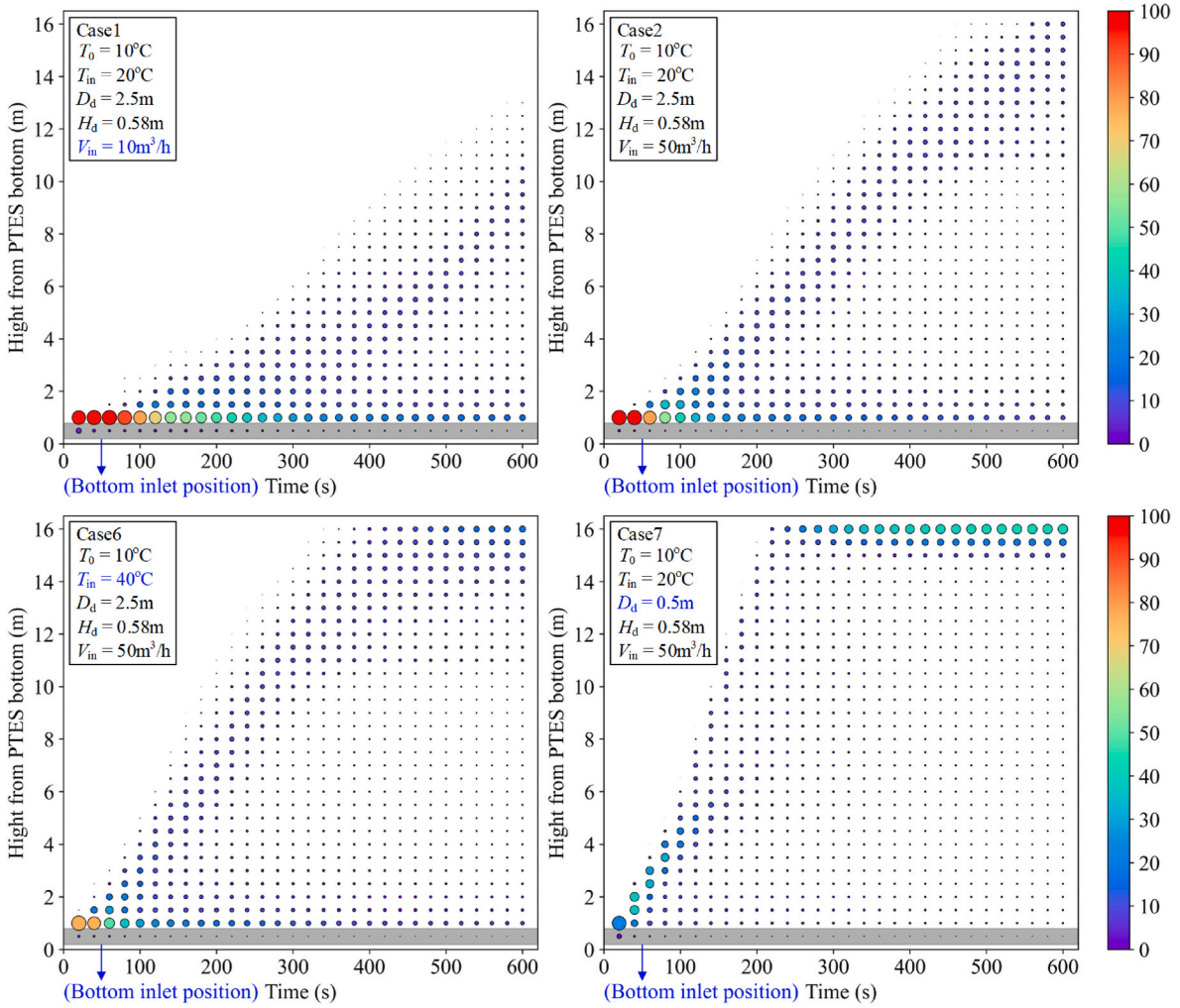

Fig. 16. Development of the energy distribution ratio under different conditions. Each circle represents the energy distribution ratio of the layer at different times.

inflow quickly spreads to the top layers, causing a sharp rise in the energy distribution ratio of the 32nd layer while maintaining a stable value of about 40%. At the same time, the energy distribution ratio of the second layer drops rapidly to below 10%.

Most of the charged heat is stored in layers either close to the bottom inlet or in the top layer of the PTES since a larger energy distribution ratio η_j is found in these layers. Therefore, efforts were made to derive the correlations of the energy distribution ratio for the second and 32nd layer based on the dimensional theory.

Fig. 17 shows the energy distribution ratio for the 2nd and the 32nd layer, respectively. All datasets can be fitted as functions in the form of Eq. (9) but with different coefficients, a and b. Combined with Fig. 16, it is evident that the start time of the energy distribution in the 32nd layer is highly affected by the inflow under different conditions, making it challenging to establish a correlation. In this case, it should be noticed that the time variable for the 32nd layer is adjusted from (t) to $(t - t_{start})$, considering the time delay associated with the start of energy distribution in that layer.

$$\eta_j = a \bullet \left(\frac{t \bullet |F| \bullet 10^{-3}}{M} \right)^b \tag{9}$$

The coefficients for these situations, along with their range of application, are listed in Table 4. The application ranges of the 2nd and 32nd layers follow the same principle. It is essential to note that the energy distribution ratio of these layers depend both on the inlet *Re* number as well as the *Fr* number. When the *Re* number is insufficiently large, it is necessary to consider the combination of *Re* number and *Fr* number.

5.3.2. *Negative buoyant jet*

The visual representation in Fig. 18 shows the cases with significant differences between the energy distribution ratio (η_j) of each layer inside the PTES. The circles are colored according to the value of the energy distribution ratio. Smaller circles represent a smaller energy distribution ratio, while larger circles represent a more significant energy distribution ratio. The layers near the middle inlet (i.e., the 22nd and 23rd layers) have a large energy distribution ratio in the first 100s. In Case 6, the energy distribution ratio of the 23rd layer is more noticeable compared to other cases. This is attributed to a significant upward penetration caused by the initial inlet momentum force being much larger than the buoyancy force. However, water at the PTES bottom for Case 6 takes longer to be affected by the inlet water because of a smaller ΔT. Moreover, the energy distribution ratio of all other layers are less than 10% during the calculation, with the exception of the layers close to the middle inlet and the PTES bottom.

Unlike the positive buoyant jets, the negative buoyant jets penetrate upward and then sink. Therefore, the fitting of the relational expression focuses on the inlet layer (22nd layer), the layer above the middle inlet (23rd layer), and the bottom layer (first layer).

Fig. 19 demonstrates the relationship between the energy distribution ratio η_j and the dimensionless time for these three layers. All data related to the 22nd and 23rd layers can be fitted as functions in the form

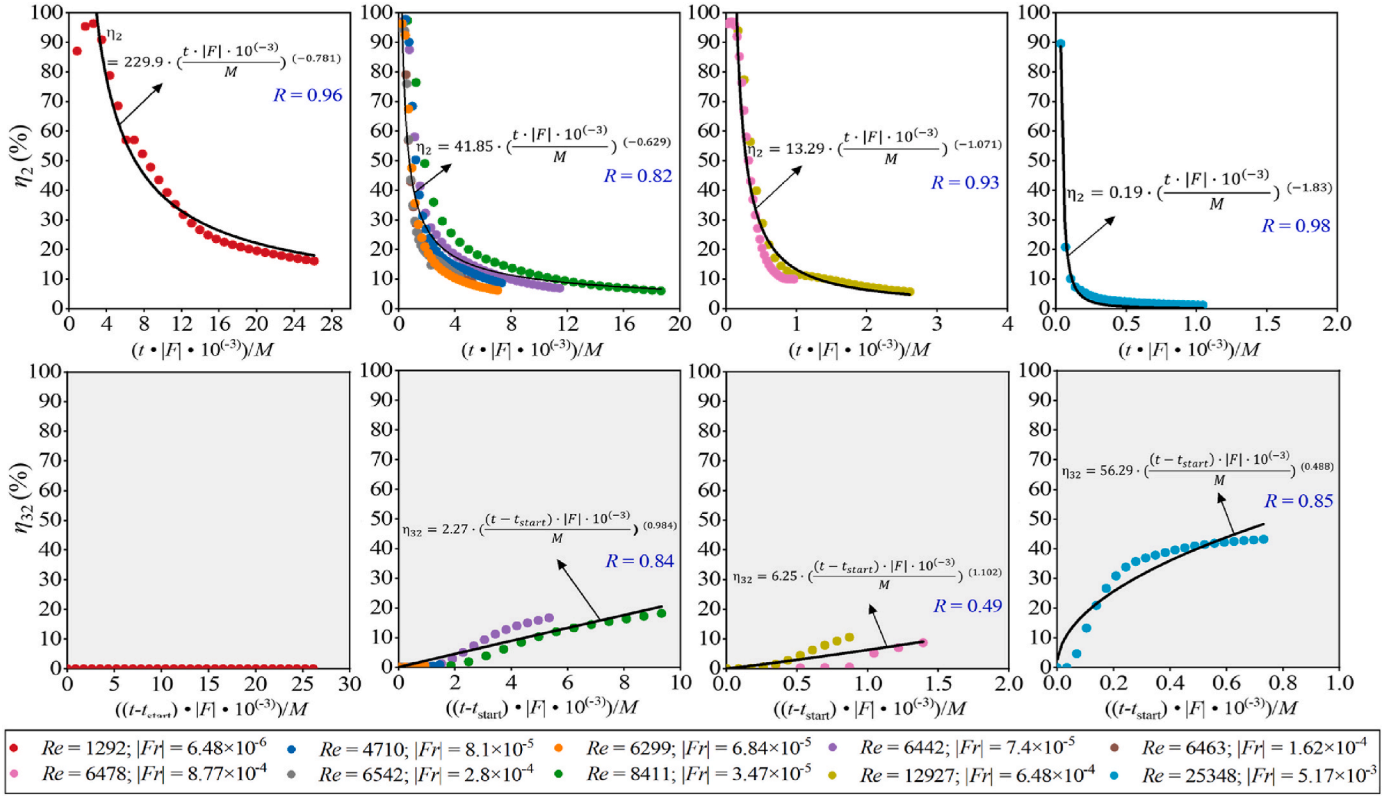

Fig. 17. Relationship between the energy distribution ratio and the dimensionless time for a positive buoyant jet (White background represents the results of the 2nd layer, and light grey background represents the results of the 32nd layer).

Table 4
Coefficients and application range for a positive buoyant jet.

Layer	Fitted equation	Coefficients		Application range
		a	b	
2nd	(9)	0.19	−0.183	$Re \geq 25{,}348$
		13.29	−1.071	$Re \geq 6478$ & $6.84 \times 10^{-4} \leq \|Fr\| \leq 8.77 \times 10^{-4}$
		41.85	−0.629	$Re > 1292$ & $\|Fr\| < 8.77 \times 10^{-4}$
		229.9	−0.781	$Re \leq 1292$
32th	(9)	56.29	0.488	$Re \geq 25{,}348$
		6.25	1.102	$Re \geq 6478$ & $6.84 \times 10^{-4} \leq \|Fr\| \leq 8.77 \times 10^{-4}$
		2.27	0.984	$Re > 1292$ & $\|Fr\| < 8.77 \times 10^{-4}$
		0	0	$Re \leq 1292$

of Eq. (10). In particular, the curve is in good agreement with the data for the 22nd and the 23rd layers, which is a consequence of the application of diffuser discs. However, it is challenging to obtain ideal correlations by fitting most of the data in the 1st layer to Eq. (9). As a result, Eq. (10) is proposed, which fits all the data perfectly (as shown in Fig. 17 (1st layer)). Detailed information related to the coefficients and application range is listed in Table 5.

$$\eta_j = a - b \bullet c^{\left(\frac{(t-t_{start}) \bullet |F| \bullet 10^{-3}}{M}\right)} \quad (10)$$

Table 5 demonstrates that the energy distribution ratio of the 23rd layer is only depending on the inlet *Re* due to the application of diffuser inlet. But for the energy distribution ratio of the 22nd and 1st layers, both inlet *Re* number and *Fr* number should be considered.

6. Discussions

6.1. Scope of application

The selection of the investigated cases is based on the actual operation of the Dronninglund project. However, the correlations of the penetration height and the energy distribution ratio are obtained based on limited datasets. Therefore, the accuracy of the expressions proposed in this study is only guaranteed with the dimensionless parameters in the ranges shown in Tables 4 and 5.

Furthermore, the model and correlations presented in this study do not consider the case of multiple diffusers serving as inlets simultaneously. As demonstrated in Table 1, when multiple diffusers are used as inlets at the same time, the proportion is only 8.18%, of which 2.94% are the top and middle diffusers working as inlets, 5.24% being the middle and bottom diffusers working as inlets. Therefore, the potential impact on the mixed region parameters is considered insignificant when multiple diffusers operate as inlets. Nevertheless, the presented model should be used with caution in this situation.

Overall, the findings of this study are derived from the fundamental dataset used in this paper. It is important to note that the correlations established in this study may need revaluation and reassessment if there are changes in the underlying data, such as the changes in PTES geometry, alteration in the inlet position along the horizontal direction, utilization of multiple diffusers as inlets simultaneously, or non-uniform initial PTES temperature distribution.

6.2. Future studies

Several gaps in this work deserve to be further studied. To quickly enrich the fundamental dataset, it is worth developing a hybrid approach that combines CFD calculation and machine learning. With this approach, the dataset may be quickly enhanced for a variety of

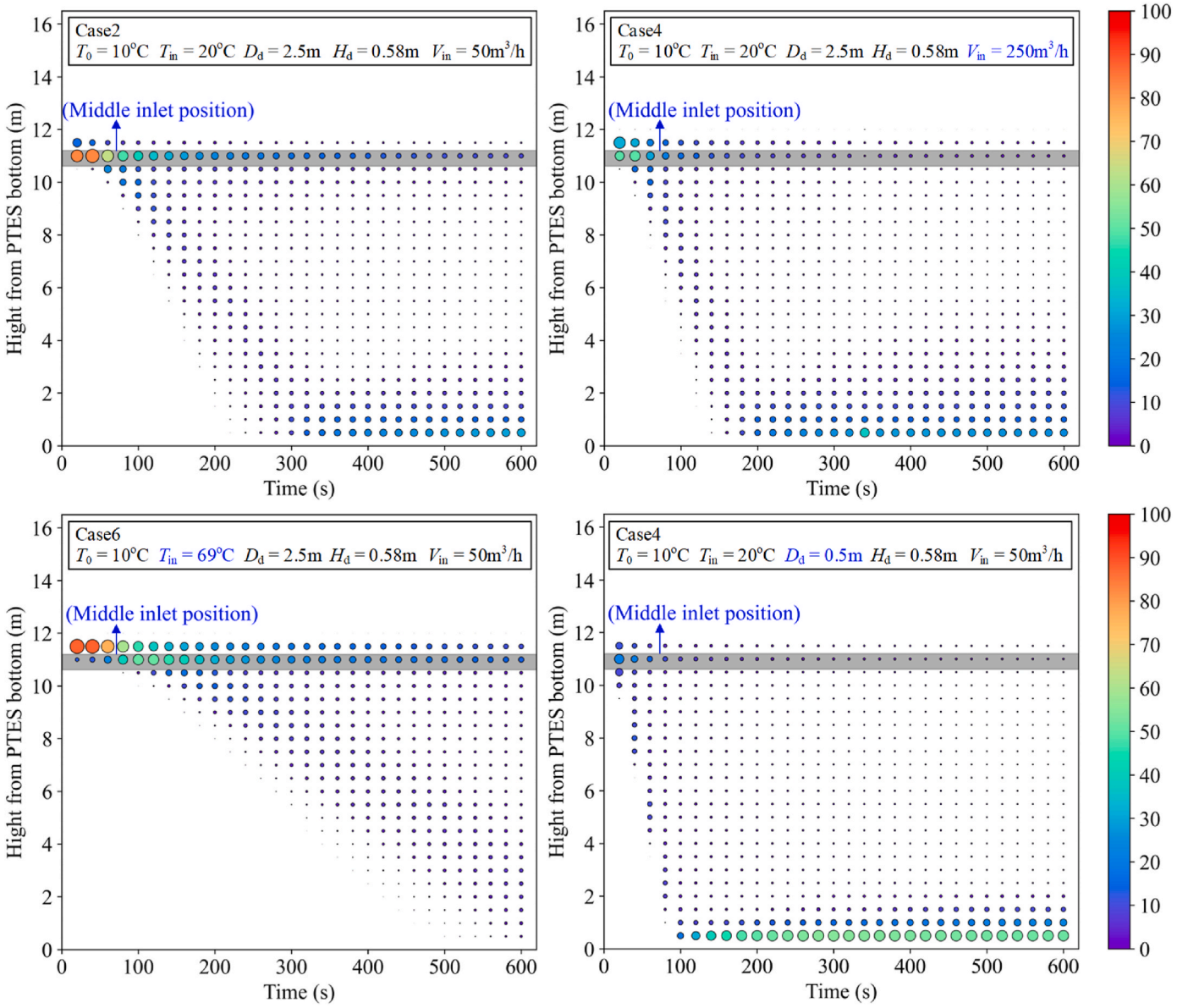

Fig. 18. Development of the energy distribution ratio under different conditions. Each circle represents the energy distribution ratio of the layer at different times.

situations, improving the accuracy and applicability of the findings. In addition, it is essential to consider the non-uniform temperature distribution of PTES under actual operating conditions. The practical significance of the study's findings can be strengthened by including suitable performance indexes for non-uniform temperature distribution, assuring their applicability in the actual PTES applications.

7. Conclusion

To accurately predict the thermal performance of the PTES, it is crucial to develop a model that is precise and efficient. The inlet mixing effect is an important aspect to be considered in this modeling process, as it has a notable impact on the thermal stratification within the PTES. Therefore, it is essential to incorporate the consideration of inlet mixing into one-dimensional numerical models of the PTES. This study explores the inlet mixing phenomenon and its impact on the overall thermal behavior of the PTES using a three-dimensional full-scale CFD model of Dronninglund PTES.

Two performance indexes are proposed in this study to quantify the mixing area inside the PTES and evaluate its influence on the energy distribution within the PTES. The following conclusions are drawn:

- For Dronninglund PTES, the bottom diffuser is used as an inlet for about 74% of the year, indicating that it is crucial to PTES's overall operating performance. The maximum temperature difference between the inflow and the water inside PTES at the level of the bottom diffuser is about 10 K. This temperature indicates the potential for significant positive buoyant jets when the bottom diffuser operates as an inlet.
- The middle diffuser is employed as an inlet roughly 16.1% of the time for Dronninglund PTES. Notably, in September and November, inflow water that is up to 30 K colder than the PTES water temperature enters the PTES. In this scenario, a strong negative buoyancy jet is expected.
- The penetration height of the inlet mixing depends on the inlet volume flow rate (V_{in}), the temperature difference between the inlet and the level of the inlet diffuser inside the PTES (ΔT), and the diffuser disc diameter (D_d).
- The dimensionless height ($Z \bullet M^{(-3/4)} \bullet |F|^{(1/2)} \bullet 10^{(-3)}$) and time ($t \bullet |F| \bullet 10^{(-3)}/M$) are still applicable for the buoyancy jet that occurs

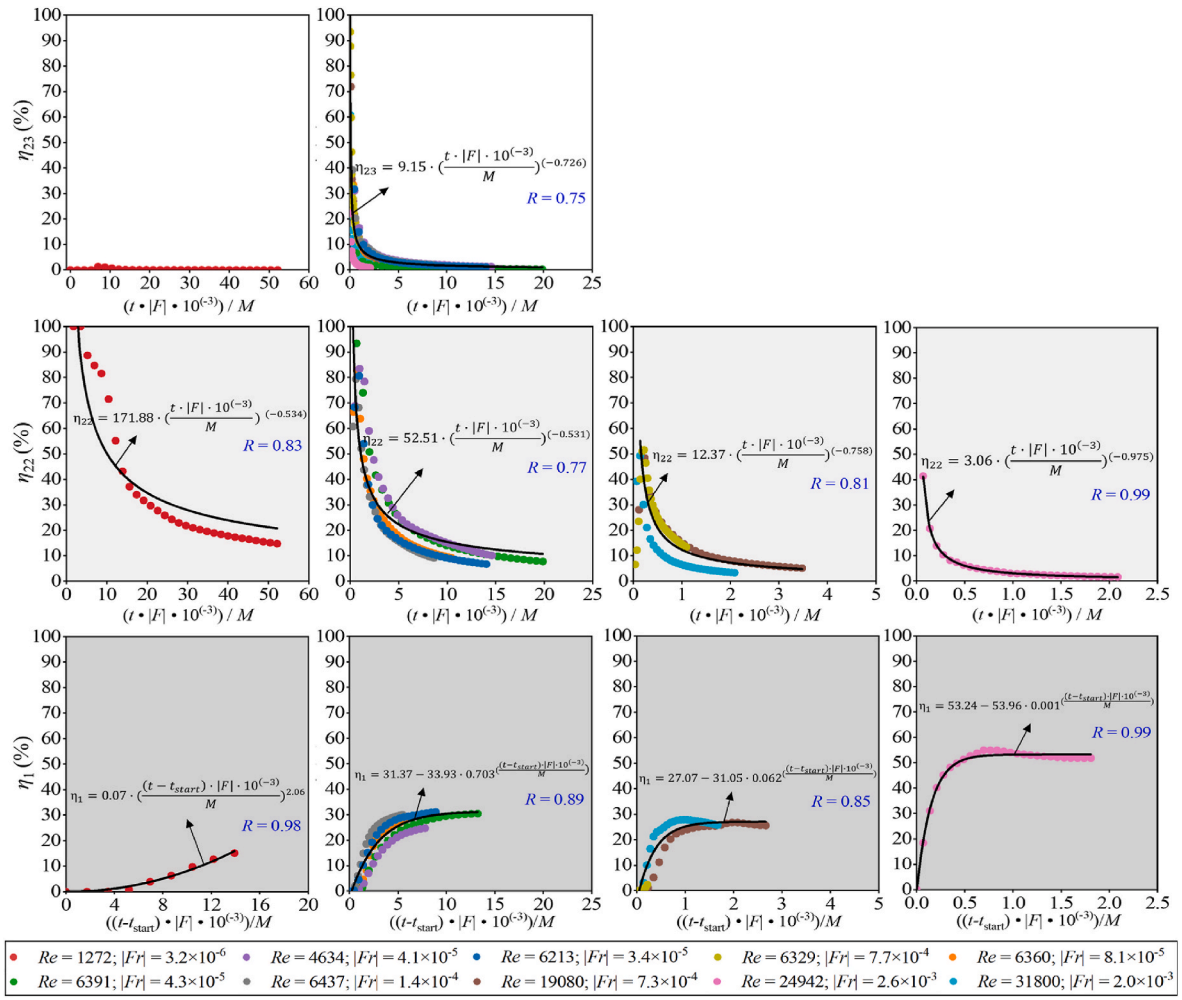

Fig. 19. Relationship between the energy distribution ratio and dimensionless time for the negative buoyant jet (White background represents the results of the 23rd layer, light grey background represents the results of the 22nd layer, and dark grey background represents the results of 1st layer).

Table 5
Coefficients and application range for the negative buoyant jet.

Layer	Fitted equation	Coefficients			Application range
		a	b	c	
1st	(10)	52.24	53.96	0.001	$Re \geq 24{,}942$ & $\lvert Fr\rvert \geq 2.6 \times 10^{-3}$
		27.07	31.05	0.062	$Re \geq 6329$ & $7.3 \times 10^{-4} \leq \lvert Fr\rvert \leq 2 \times 10^{-3}$
		31.37	33.93	0.703	$Re > 1272$ & $\lvert Fr\rvert < 7.3 \times 10^{-4}$
	(9)	0.07	2.06	-	$Re \leq 1272$
22th	(9)	3.06	−0.975	-	$Re \geq 24{,}942$ & $\lvert Fr\rvert \geq 2.6 \times 10^{-3}$
		12.37	−0.758		$Re \geq 6329$ & $7.3 \times 10^{-4} \leq \lvert Fr\rvert \leq 2 \times 10^{-3}$
		52.51	−0.531	-	$Re > 1272$ & $\lvert Fr\rvert < 7.3 \times 10^{-4}$
		171.88	−0.534	-	$Re \leq 1272$
23th	(9)	9.15	0.726	-	$Re > 1272$
		0	0	-	$Re \leq 1272$

within PTES. These dimensionless quantities are typically fitted using a power law relationship, allowing for a more comprehensive characterization of the penetration height and time-dependent behavior. In addition, the correlations derived from this study reveal that the transient dimensionless penetration height is primarily dependent on the inlet *Re* number for both the positive and negative buoyancy jets.

- For the positive buoyancy jet, the most thermally influenced layers of the PTES are the layers near the bottom inlet (2nd layer) and the top layer (32nd layer). The energy distribution ratio can be found for a layer using the formula $\eta_j = a \bullet (t \bullet |F| \bullet 10^{(-3)}/M)^b$, however the coefficients vary with the *Re* number and the *Fr* number.
- For the negative buoyancy jet, the middle inlet layer (22nd layer), the layer just above the middle inlet (23rd layer), and the bottom layer (1st layer) experience the most significant thermal influence. The energy distribution ratio formula, $\eta_j = a \bullet (t \bullet |F| \bullet 10^{(-3)}/M)^b$, is suitable for the 22nd and 23rd layers. However, a slightly modified formula $\eta_j = a - b \bullet c^{t \bullet |F| \bullet 10^{(-3)}/M}$ provides a good representation of the jet influence for the 1st layer and accounts for its specific characteristics.

In conclusion, this study emphasis the significance of understanding and quantifying the influence of inlet mixing on the PTES performance. Researchers and engineers can gain valuable insights into the thermal dynamics of PTES and make well-informed decisions about its design and operation by utilizing the suggested performance indicators. Furthermore, the proposed correlations can be used to improve existing one-dimensional PTES models targeting higher prediction accuracy of thermal stratification in the heat storage.

CRediT authorship contribution statement

Yutong Xiang: Research, Writing – original draft. **Meng Gao:** Writing – review & editing. **Simon Furbo:** Supervision, Writing – review & editing. **Jianhua Fan:** Funding acquisition, idea formulation, Writing – review & editing. **Gang Wang:** Writing – review & editing. **Zhiyong Tian:** Writing – review & editing. **Dengjia Wang:** Writing – review & editing.

Declaration of competing interest

We confirm that the manuscript has been read and approved by all named authors and that there are no other persons who satisfied the criteria for authorship but are not listed. We further confirm that the order of authors listed in the manuscript has been approved by all of us.

We confirm that we have given due consideration to the protection of intellectual property associated with this work and that there are no impediments to publication, including the timing of publication, with respect to intellectual property. In so doing we confirm that we have followed the regulations of our institutions concerning intellectual property.

We understand that the Corresponding Author is the sole contact for the Editorial process (including Editorial Manager and direct communications with the office). He/she is responsible for communicating with the other authors about progress, submissions of revisions and final approval of proofs. We confirm that we have provided a current, correct email address which is accessible by the Corresponding Author.

Acknowledgments

The work is partly funded by the Danish Energy Agency EUDP project titled Participation in the IEA SHC Task 68 on “Efficient Solar District Heating Systems” (no. 134-21027) and the Chinese Scholarship Council (CSC). Without their support, the research would not be possible.

References

[1] International Energy Agency, World Energy Outlook, 2022.
[2] D. Gao, T.H. Kwan, Y.N. Dabwan, M. Hu, Y. Hao, T. Zhang, et al., Seasonal-regulatable energy systems design and optimization for solar energy year-round utilization, Appl. Energy 322 (2022), 119500, https://doi.org/10.1016/j.apenergy.2022.119500.
[3] Y. Xiang, Z. Xie, S. Furbo, D. Wang, J. Fan, A comprehensive review on pit thermal energy storage: technical elements, numerical approaches and recent applications, J. Energy Storage 55 (2022), 105716, https://doi.org/10.1016/j.est.2022.105716.
[4] P. Tatsidjodoung, N. Le Pierrès, L. Luo, A review of potential materials for thermal energy storage in building applications, Renew. Sustain. Energy Rev. 18 (2013) 327–349, https://doi.org/10.1016/j.rser.2012.10.025.
[5] J. Fan, S. Furbo, Thermal stratification in a hot water tank established by heat loss from the tank, Sol. Energy 86 (2012) 3460–3469, https://doi.org/10.1016/j.solener.2012.07.026.
[6] Q. Li, W. Lin, X. Huang, Y. Tai, X. Ding, Y. Zhang, Thermocline dynamics in a thermally stratified water tank under different operation modes, Appl. Therm. Eng. 212 (2022), 118560, https://doi.org/10.1016/j.applthermaleng.2022.118560.
[7] I. Sifnaios, A.R. Jensen, S. Furbo, J. Fan, Performance comparison of two water pit thermal energy storage (PTES) systems using energy, exergy, and stratification indicators, J. Energy Storage 52 (2022), 104947, https://doi.org/10.1016/j.est.2022.104947.
[8] H.O. Njoku, O.V. Ekechukwu, S.O. Onyegegbu, Analysis of stratified thermal storage systems: an overview, Heat Mass Tran. 50 (2014) 1017–1030, https://doi.org/10.1007/s00231-014-1302-8.
[9] S. Alizadeh, An experimental and numerical study of thermal stratification in a horizontal cylindrical solar storage tank, Sol. Energy 66 (1999) 409–421, https://doi.org/10.1016/S0038-092X(99)00036-5.
[10] Y.M. Han, R.Z. Wang, Y.J. Dai, Thermal stratification within the water tank, Renew. Sustain. Energy Rev. 13 (2009) 1014–1026, https://doi.org/10.1016/j.rser.2008.03.001.
[11] M.A. Karim, Experimental investigation of a stratified chilled-water thermal storage system, Appl. Therm. Eng. 31 (2011) 1853–1860, https://doi.org/10.1016/j.applthermaleng.2010.12.019.
[12] Z. Lavan, J. Thompson, Experimental study of thermally stratified hot water storage tanks, Sol. Energy 19 (1977) 519–524, https://doi.org/10.1016/0038-092X(77)90108-6.
[13] K. Hariharan, K. Badrinarayana, S. Srinivasa Murthy, M.V. Krishna Murthy, Temperature stratification in hot-water storage tanks, Energy 16 (1991) 977–982, https://doi.org/10.1016/0360-5442(91)90057-S.
[14] Y. Deng, D. Sun, M. Niu, B. Yu, R. Bian, Performance assessment of a novel diffuser for stratified thermal energy storage tanks – the nonequal-diameter radial diffuser, J. Energy Storage 35 (2021), https://doi.org/10.1016/j.est.2021.102276.
[15] A. Zachár, I. Farkas, F. Szlivka, Numerical analyses of the impact of plates for thermal stratification inside a storage tank with upper and lower inlet flows, Sol. Energy 74 (2003) 287–302, https://doi.org/10.1016/S0038-092X(03)00188-9.
[16] L.J. Shah, S. Furbo, Entrance effects in solar storage tanks, Sol. Energy 75 (2003) 337–348, https://doi.org/10.1016/j.solener.2003.04.002.
[17] Y.H. Zurigat, A.J. Ghajar, E.M. Moretti, Stratified thermal storage tank inlet mixing characterization, Appl. Energy 30 (1988) 99–111.
[18] J.D. Chung, S.H. Cho, C.S. Tae, H. Yoo, The effect of diffuser configuration on thermal stratification in a rectangular storage tank, Renew. Energy 33 (2008) 2236–2245, https://doi.org/10.1016/j.renene.2007.12.013.
[19] C.K. Yee, F.C. Lai, Effects of a porous manfold on thermal stratification in a liquid storage tank, Sol. Energy 71 (2001) 241–254, https://doi.org/10.1016/S0038-092X(01)00043-3.
[20] E. Andersen, S. Furbo, J. Fan, Multilayer fabric stratification pipes for solar tanks, Sol. Energy 81 (2007) 1219–1226, https://doi.org/10.1016/j.solener.2007.01.008.
[21] L.J. Shah, E. Andersen, S. Furbo, Theoretical and experimental investigations of inlet stratifiers for solar storage tanks, Appl. Therm. Eng. 25 (2005) 2086–2099, https://doi.org/10.1016/j.applthermaleng.2005.01.011.
[22] F. Findeisen, T. Urbaneck, B. Platzer, Radial diffusers in stratified hot water stores: geometry optimization with CFD, ISES Solar World Congress 2017 (2017) 726–734, https://doi.org/10.18086/swc.2017.13.04.
[23] F. Findeisen, T. Urbaneck, B. Platzer, Radial diffusers – simulation of three-dimensional flow effects with CFD (Part 1), Chemie Ingenieur Technik. 90 (2018) 956–968, https://doi.org/10.1002/cite.201700023.
[24] F. Findeisen, T. Urbaneck, B. Platzer, Radial diffusers - simulation of three-dimensional flow effects with CFD (Part 2), Chemie Ingenieur Technik. 90 (2018) 1065–1072, https://doi.org/10.1002/cite.201700126.
[25] F. Findeisen, T. Urbaneck, B. Platzer, Radial diffusers – simulation of three-dimensional flow effects with CFD (Part 3), Chemie Ingenieur Technik. 90 (2018) 969–978, https://doi.org/10.1002/cite.201700070.
[26] F. Findeisen , K. Ullrich, T. Urbaneck, B. Platzer. Radial diffusers in stratified hot water stores: simulation of three-dimensional flow behavior with CFD, 5th International Solar District Heating Conference. (2018) 120-126.
[27] D.J. Nizami, M.F. Lightstone, S.J. Harrison, C.A. Cruickshank, Negative buoyant plume model for solar domestic hot water tank systems incorporating a vertical inlet, Sol. Energy 87 (2013) 53–63, https://doi.org/10.1016/j.solener.2012.10.001.
[28] F.J. Oppel, A.J. Ghajar, P.M. Moretti, A numerical and experimental study of stratified thermal storage, Build. Eng. 92 (1986) 293–309.
[29] Y.H. Zurigat, P.R. Liche, A.J. Ghajar,Turbulent mixing correclations for a thermocline thermal storage tank, Heat Transfer 84 (1988) 160-168.
[30] N.M. Al-Najem, M.M. El-Refaee, A numerical study for the prediction of turbulent mixing factor in thermal storage tanks, Appl. Therm. Eng. 17 (1997) 1173–1181, https://doi.org/10.1016/s1359-4311(97)00030-6.
[31] J.E.B. Nelson, A.R. Balakrishnan, S. Srinivasa Murthy, Experiments on stratified chilled-water tanks, Int. J. Refrig. 22 (1999) 216–234, https://doi.org/10.1016/S0140-7007(98)00055-3.
[32] A. Karim, A. Burnett, S. Fawzia, Investigation of stratified thermal storage tank performance for heating and cooling applications, Energies 11 (2018), https://doi.org/10.3390/en11051049.
[33] U. Jordan, S. Furbo, Thermal stratification in small solar domestic storage tanks caused by draw-offs, Sol. Energy 78 (2005) 291–300, https://doi.org/10.1016/j.solener.2004.09.011.
[34] B. Baeten, T. Confrey, S. Pecceu, F. Rogiers, L. Helsen, A validated model for mixing and buoyancy in stratified hot water storage tanks for use in building energy simulations, Appl. Energy 172 (2016) 217–229, https://doi.org/10.1016/j.apenergy.2016.03.118.
[35] J.H. Davidson, D.A. Adams, J.A. Miller, A coefficient to characterize mixing in solar water storage tanks, J. Sol. Energy Eng. 116 (1994) 94–99, https://doi.org/10.1115/1.2930504.
[36] C. Winterscheid, Dronninglund district heating monitaring data evaluation for the Years 2015-2017, 2017.
[37] G. Gauthier, PlanEnergi, Benchmarking and improving models of subsurface heat storage dynamics, comparison of Danish PTES and BTES installation measurements with their corresponding TRNSYS models. https://www.heatstore.eu/documents/HEATSTORE_WP2_D2.3-Danish%20PTES%20and%20BTES%20installations_Final_2020.11.02.pdf.
[38] A. Sørensen, T. Schmidt, Design and construction of large scale heat storages for district heating in Denmark, 14th International Conference on Energy Storage, Turkey, 2018.
[39] A.V. Novo, J.R. Bayon, D. Castro-Fresno, J. Rodriguez-Hernandez, Review of seasonal heat storage in large basins: water tanks and gravel-water pits, Appl. Energy 87 (2010) 390–397, https://doi.org/10.1016/j.apenergy.2009.06.033.
[40] F. Ochs, J. Nußbicker, R. Marx, H. Koch, W. Heidemann, H. Müller-Steinhagen, Solar assisted district heating system with seasonal thermal energy storage in Eggenstein-Leopoldshafen, EuroSun 2008. (2008) Lisboa.
[41] C. Chang, G. Leng, C. Li, B. Nie, X. She, X. Peng, et al., Investigation on transient cooling process in a water heat storage tank with inclined sidewalls, Energy Proc. 142 (2017) 142–147, https://doi.org/10.1016/j.egypro.2017.12.023.

[42] K. Osman, S.M.N. Al Khaireed, M.K. Ariffin, M.Y. Senawi, Dynamic modeling of stratification for chilled water storage tank, Energy Convers. Manag. 49 (2008) 3270–3273, https://doi.org/10.1016/j.enconman.2007.09.035.
[43] Y.P. Chandra, T. Matuska, Stratification analysis of domestic hot water storage tanks: a comprehensive review, Energy Build. 187 (2019) 110–131, https://doi.org/10.1016/j.enbuild.2019.01.052.
[44] W. Lou, L. Luo, Y. Hua, Y. Fan, Z. Du, A review on the performance indicators and influencing factors for the thermocline thermal energy storage systems, Energies 14 (2021) 1–19, https://doi.org/10.3390/en14248384.
[45] J. Song, W.P. Bahnfleth, J.M. Cimbala, Parametric study of single-pipe diffusers in stratified chilled water storage tanks (RP-1185), HVAC&R Research. 10 (2004) 345–365, https://doi.org/10.1080/10789669.2004.10391108.
[46] Y. Xiang, M. Gao, S. Furbo, D. Wang, Z. Tian, J. Fan, Heat transfer of a large-scale water pit heat storage under transient operations, J. Energy Storage 55 (2022), 105455, https://doi.org/10.1016/j.est.2022.105455.
[47] C. Xu, M. Liu, S. Jiao, H. Tang, J. Yan, Experimental study and analytical modeling on the thermocline hot water storage tank with radial plate-type diffuser, Int. J. Heat Mass Tran. 186 (2022), https://doi.org/10.1016/j.ijheatmasstransfer.2021.122478.
[48] J. Rendall, A. Abu-Heiba, K. Gluesenkamp, K. Nawaz, W. Worek, A. Elatar, Nondimensional convection numbers modeling thermally stratified storage tanks: Richardson's number and hot-water tanks, Renew. Sust. Energ. Rev. 150 (2021), 111471, https://doi.org/10.1016/j.rser.2021.111471.
[49] J.S. Turner, Jets and plumes with negative or reversing buoyancy, J. Fluid Mech. 26 (1966) 779–792, https://doi.org/10.1017/S0022112066001526.
[50] J.S. Turner, Turbulent entrainment the development of the entrainment assumption, and its application to geophysical flows, J. Fluid Mech. 173 (1986) 431–471.
[51] J.H. Middleton, The asymptotic behaviour of a starting plume, J. Fluid Mech. 72 (1975) 753–771, https://doi.org/10.1017/S0022112075003266.